NASA/TP-20230006306

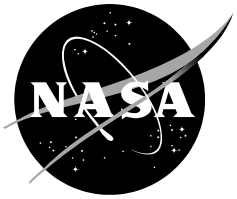

NAIRAS Ionizing Radiation Model: Extension from Atmosphere to Space

Christopher J. Mertens
Langley Research Center, Hampton, Virginia

Guillaume P. Gronoff and Daniel Phoenix
Science Systems and Applications (SSAI), Inc., Hampton, Virginia

Yihua Zheng and Maksym Petrenko
Goddard Space Flight Center, Greenbelt, Maryland

Janessa Buhler
Kennedy Space Center, Merritt Island, Florida

Insoo Jun
Jet Propulsion Laboratory, Pasadena, California

Joseph Minow and Emily Willis
Marshall Space Flight Center, Huntsville, Alabama

May 2023

NASA STI Program Report Series

The NASA STI Program collects, organizes, provides for archiving, and disseminates NASA's STI. The NASA STI program provides access to the NTRS Registered and its public interface, the NASA Technical Reports Server, thus providing one of the largest collections of aeronautical and space science STI in the world. Results are published in both non-NASA channels and by NASA in the NASA STI Report Series, which includes the following report types:

- TECHNICAL PUBLICATION. Reports of completed research or a major significant phase of research that present the results of NASA Programs and include extensive data or theoretical analysis. Includes compilations of significant scientific and technical data and information deemed to be of continuing reference value. NASA counterpart of peer-reviewed formal professional papers but has less stringent limitations on manuscript length and extent of graphic presentations.

- TECHNICAL MEMORANDUM. Scientific and technical findings that are preliminary or of specialized interest, e.g., quick release reports, working papers, and bibliographies that contain minimal annotation. Does not contain extensive analysis.

- CONTRACTOR REPORT. Scientific and technical findings by NASA-sponsored contractors and grantees.

- CONFERENCE PUBLICATION. Collected papers from scientific and technical conferences, symposia, seminars, or other meetings sponsored or co-sponsored by NASA.

- SPECIAL PUBLICATION. Scientific, technical, or historical information from NASA programs, projects, and missions, often concerned with subjects having substantial public interest.

- TECHNICAL TRANSLATION. English-language translations of foreign scientific and technical material pertinent to NASA's mission.

Specialized services also include organizing and publishing research results, distributing specialized research announcements and feeds, providing information desk and personal search support, and enabling data exchange services.

For more information about the NASA STI program, see the following:

- Access the NASA STI program home page at http://www.sti.nasa.gov

- Help desk contact information:

https://www.sti.nasa.gov/sti-contact-form/ and select the "General" help request type.

NASA/TP-20130006306

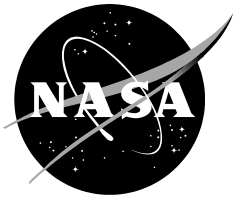

NAIRAS Ionizing Radiation Model: Extension from Atmosphere to Space

Christopher J. Mertens
Langley Research Center, Hampton, Virginia

Guillaume P. Gronoff and Daniel Phoenix
Science Systems and Applications (SSAI), Inc., Hampton, Virginia

Yihua Zheng and Maksym Petrenko
Goddard Space Flight Center, Greenbelt, Maryland

Janessa Buhler
Kennedy Space Center, Florida

Insoo Jun
Jet Propulsion Laboratory, Pasadena, California

Joseph Minow and Emily Willis
Marshall Space Flight Center, Huntsville, Alabama

National Aeronautics and
Space Administration

Langley Research Center
Hampton, Virginia, 23681-2199

May 2023

Acknowledgments

The NAIRAS model extension from the atmosphere to space and the transition of the model to the NASA Goddard Space Flight Center's Community Coordinated Modeling Center (CCMC) were funded by the NASA Engineering and Safety Center (NESC) assessment TI-19-01468. The improvements in solar energetic particle (SEP) event spectral fitting and geomagnetic vertical cutoff rigidity modeling were funded by the NASA Science Mission Directorate, Heliophysics Division, Space Weather Science Applications Program.

This report is available in electronic form at

http://

Abstract

The Nowcast of Aerospace Ionizing RAdiation System (NAIRAS) model is a real-time, global, physics-based model originally developed to predict exposure from cosmic radiation to air travelers from both galactic and solar sources. A prototype operational NAIRAS model has provided tabular and graphical data products via its public web site for about ten years. A new version of the NAIRAS model has been developed that incorporates an extension of the model domain from the atmospheric ionizing radiation environment to the space radiation environment, with the addition of the trapped inner belt proton source and altitude-dependent and rigidity-dependent geomagnetic shielding of the galactic cosmic rays (GCR) and solar energetic particle (SEP) protons. New output products of differential and integral particle flux have been developed for the characterization of single-event effects (SEE), expanding the application of NAIRAS from human radiation exposure assessment to allowing end-users to quantify radiation environment risks to aviation and spacecraft microelectronic systems. The NAIRAS model has transitioned to prototype operations at the Community Coordinated Modeling Center (CCMC) where the model now operates in two modes: (1) real-time global predictions of the atmospheric radiation environment and (2) a run-on-request (RoR) service allowing the user to select a specific time period for the global dosimetric calculations, or to upload an aircraft, balloon, or spaceflight trajectory file to provide predictions of the dosimetric and particle flux quantities along the flight path. The new features of NAIRAS version 3.0 are described in this paper and example results of the new output products for low-Earth orbit (LEO), medium-Earth orbit (MEO), and free-space radiation environments are presented.

1.0 Introduction

The Nowcast of Aerospace Ionizing RAdiation System (NAIRAS) is composed of coupled physics-based models that transport cosmic radiation through the heliosphere, Earth's magnetosphere, the neutral atmosphere, and aircraft or spacecraft shielding. Two extraterrestrial sources of ionizing radiation are included: (1) ubiquitous galactic cosmic rays (GCR) originating from outside the solar system, and (2) solar energetic particle (SEP) protons originating from transient solar storm events (Mertens et al., 2010, 2012, 2013). The transport through the magnetosphere incorporates the dynamical response of the geomagnetic field to space weather variability in the interplanetary medium (Kress et al., 2010; Mertens et al., 2010). Transport of cosmic radiation through material media – i.e., the atmosphere and/or aircraft or spacecraft shielding – is calculated with the deterministic HZETRN transport code (Wilson et al, 1991, 2005; Slaba et al., 2020b). Thus, the NAIRAS model computes ionizing radiation particle flux spectra from the primary sources and the secondary radiations produced from nuclear interactions between the radiation source ions and the constituents of the intervening material media. The secondary particles consist of heavy-ion fragments from GCR ions, projectile and target light-ions, neutrons, pions and muons, and electromagnetic cascade particles (electrons, positrons, and gamma ray photons) (Mertens, 2016a) produced by interactions of the material media with both GCR and SEP primary particles. The particle flux spectra are the fundamental physical quantities from which important response functions are calculated, such as dosimetric quantities and various flux quantities useful for characterizing single-event effects (SEE).

The NAIRAS model was originally developed to provide real-time predictions of dosimetric quantities to quantify human radiation exposure at aviation altitudes (Mertens et al., 2010, 2012,

2013). The model has been running on the NASA Langley Research Center (LaRC) computer cluster and output graphical and tabular data products are hosted on Space Environment Technologies, Inc. server/website (http://sol.spacenvironment.net/~nairas/). The key features of the real-time NAIRAS model are: 1) global maps of characteristics of the atmospheric ionizing radiation environment provided at an hourly cadence on a 1x1 degree latitude/longitude grid, 0-90 km in altitude at 1 km increments; 2) both GCR and SEP sources of atmospheric ionizing radiation are included in real-time; 3) computation of radiation transport through material media is physics-based using the deterministic HZETRN code; and 4) the temporal and spatial variations in geomagnetic transmission of GCR and SEP primary particle spectra due to coupling between the magnetosphere and the interplanetary plasma environment are also included in real-time.

The focus of this paper is the description of the new developments incorporated into NAIRAS version 3.0. The model altitude domain has been extended above the neutral atmosphere into the geospace and free-space radiation environments for the assessment of SEE in spacecraft microelectronic systems. The model domain extension necessarily required the addition of a trapped inner belt proton model to the suite of NAIRAS radiation environment model components. Moreover, in the geospace environment the vertical cutoff rigidity alone is not adequate to parameterize the geomagnetic transmission of free-space GCR and SEP primary particle spectra through the magnetosphere, which is the customary approximation for the atmospheric ionizing radiation environment. Thus, the NAIRAS model was updated to include an altitude-dependent and rigidity-dependent geomagnetic transmission function. New differential and integral flux quantities have been developed and added to the model output for the characterization of SEE. Thus, the new output quantities have expanded the application of the NAIRAS model from human radiation exposure assessments to the quantification of radiation effects on spacecraft microelectronic systems. The NAIRAS code has been transitioned to prototype operations at the Community Coordinated Modeling Center (CCMC) where the new version 3.0 capabilities are available to the public (https://ccmc.gsfc.nasa.gov/models/NAIRAS~3.0).

The new developments in NAIRAS version 3.0 are presented in the remainder of the paper. The new data products for SEE assessment and the user interface are described in more detail in section 2. The model improvements and enhancements are summarized in section 3. Examples of the new output quantities for low-Earth orbit (LEO), medium-Earth orbit (MEO), and free-space spaceflight trajectories are presented in section 4. Summary and conclusions are provided in section 5.

2.0 NAIRAS Output Products and User Interface

The NAIRAS code has been transitioned to prototype operations at CCMC where the model operates in two independent modes: (1) real-time global predictions of the atmospheric radiation environment, which are updated hourly, and (2) a run-on-request (RoR) capability allowing the user to select a specific time period for the global dosimetric calculations, or to upload an aircraft, balloon, or spaceflight trajectory file to provide simulations of the dosimetric and particle flux quantities along the input flight path. The NAIRAS RoR service operates in quasi real-time in the sense that the datetime of a RoR run job can be from the previous day.

The graphical products from the real-time, global operation mode are available via the CCMC Integrated Space Weather Analysis System (iSWA). A screenshot of an example of the NAIRAS real-time products from iSWA is shown in Figure 1.

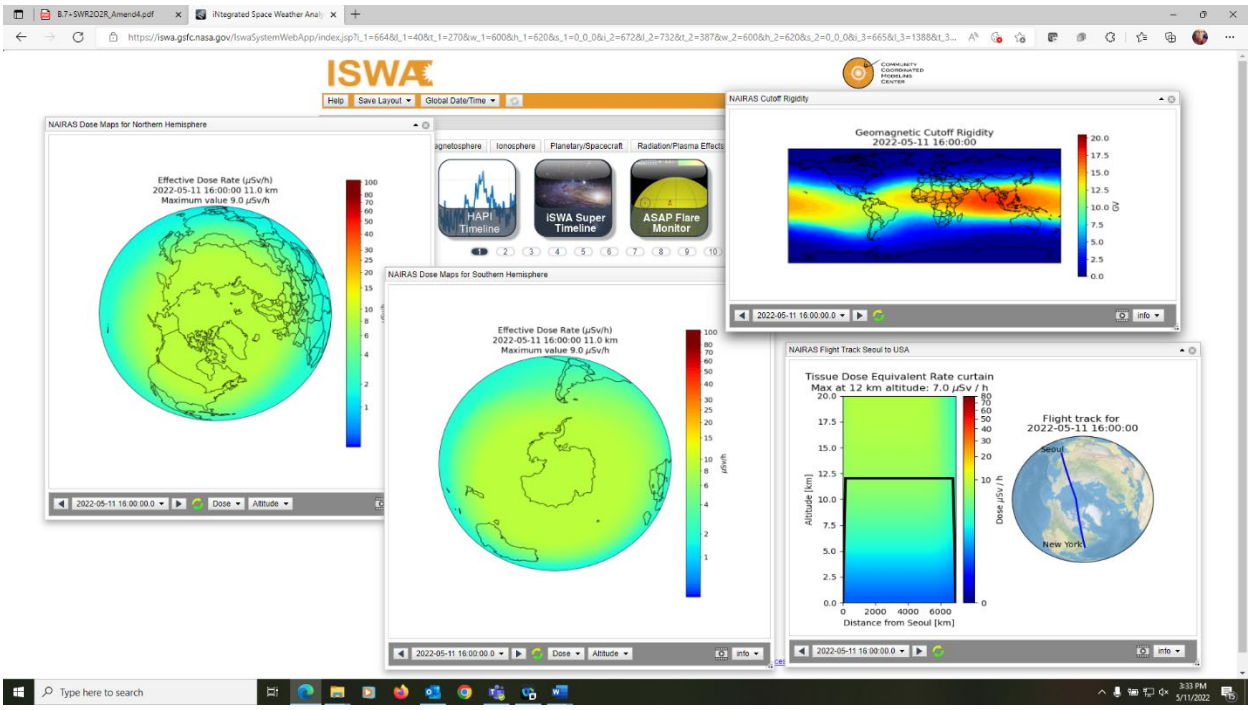

Figure 1: Screenshot of example NAIRAS real-time graphical products at CCMC/iSWA located under the Radiation/Plasma Effects tab (https://iswa.gsfc.nasa.gov/IswaSystemWebApp/). The left panel is northern hemisphere effective dose rate (uSv/h). The bottom center panel is southern hemisphere effective dose rate (uSv/h). The upper right panel is vertical geomagnetic cutoff rigidity (GV). The right bottom panel shows a vertical slice of dose equivalent rate (uSv/h) for a high-latitude commercial flight from New York to Seoul.

The left panel in Figure 1 is effective dose rate over the northern hemisphere for the latest hourly prediction. Dose rates from a southern hemisphere view are also shown in the bottom center panel. The user can select prior hourly predictions going back to year 2020 when NAIRAS became operational at iSWA. The user can select five dosimetric quantities: absorbed dose in silicon, absorbed dose in tissue, dose equivalent, ambient dose equivalent, and effective dose. The definitions of these quantities and their relevance in characterizing the ionizing radiation environment are summarized in Mertens (2016a). The user can select four barometric altitudes for displaying the dosimetric quantities: 5 km, 11 km, 15 km, and 40 km. The cruising altitude of small aircraft and commercial flights are largely bound by the altitude range 5-11 km. Corporate aircraft cruising altitudes are typically between 12-15 km. The highest altitude of 40 km provides a reasonable proxy for free-space ionizing radiation exposure behind the typical shielding of an aircraft/spacecraft (~ 3-5 g/cm^2 aluminum-equivalent (Singleterry et al., 1999; Hu et al., 2009; Townsend et al., 2018), which when converted to an equivalent atmospheric depth corresponds to ~ 40 km in the U.S. Standard Atmosphere). The upper right panel is the vertical geomagnetic cutoff rigidity for the latest hourly dose predictions in this example. The right bottom panel is a vertical slice of dose equivalent rate for a commercial flight from New York to Seoul.

The RoR capability allows the user to run the NAIRAS model for customized application scenarios and time periods. These features are summarized in Table 1. The global dosimetric

run option mirrors the execution of the real-time mode of the NAIRAS model for a user-specified time period. The input is simply start and end datetime for the model run. The output quantities are the same five dosimetric quantities provided by the real-time run mode. Hourly output files of the dosimetric quantities calculated at each model grid point described previously are written out over the duration of the user-input start/end datetime interval. This class of run option capability provides global context and situational awareness of the atmospheric ionizing radiation environment. Furthermore, retrospective scientific analysis and verification and validation of the real-time mode of the NAIRAS model can be readily performed.

Table 1: RoR Capability Summary and Description (see text for details).

Run Option	Output Quantities		User Input
Global Dosimetric	Absorbed dose in silicon, absorbed dose in tissue, dose equivalent, ambient dose equivalent, effective dose		Start/End Date-Time
Flight Trajectory	**Dosimetric and Flux/Fluence**		Trajectory file (date/time/lat/lon/alt)
	Dosimetric	Same as above	Shielding depths for dosimetric calculations
	Flux/Fluence		Shielding depths for flux/fluence calculations
		Integral • GCR LET • SEP proton • TRP proton	Lower LET/energy bounds
		Differential • GCR LET • SEP proton • TRP proton	N/A (full model differential spectra written to output)

The RoR flight trajectory run option allows the user to upload a trajectory file. The model output products are calculated at each trajectory point. Also available to the user are the output quantities time-integrated over the duration of the flight. The trajectory file can correspond to an aircraft, balloon, or spacecraft flight. The key input fields of the trajectory file are date, time, geographic latitude and longitude, and altitude. The datetime format of the trajectory file can be either Gregorian or modified Julian date. The user can select any combination of dosimetric and differential and integral flux and fluence quantities listed in the Table 1. The dosimetric outputs are the same five quantities available from the real-time NAIRAS operation mode or from the RoR global dosimetric run option. The flux and fluence output products are quantities useful for assessing SEE. Differential and integral linear-energy transfer (LET) flux and fluence quantities are calculated from the GCR radiation source. Differential and integral proton flux and fluence quantities are calculated from the SEP and trapped proton (TRP) radiation sources. For the calculation of the integral LET (GCR) and proton (SEP/TRP) flux and fluence quantities, the user can select as many output quantities as desired, which are defined by the user-specified threshold LET (GCR) or proton (SEP/TRP) energy of the associated integral quantity. The user can input as many aluminum-equivalent shielding depths as needed at which the selected output quantities are calculated. Two separate sets of shielding depths can be specified for the dosimetric and flux/fluence quantities. These two sets allow detailed model comparisons to onboard dosimeters or crew member locations, characterized by unique shielding environments, and radiation environment characterization at the shielded location of individual microelectronic components via the flux/fluence quantities that can be imported into SEE assessment applications.

3.0 NAIRAS Model Improvements

The NAIRAS model updates and enhancements in version 3.0 are described in this section. For each model component, a summary of the previous version is given followed by a more detailed description of the new features and improvements. The key model components are described in the subsections, which are ordered according to the chain of transport and interactions from radiation source to output radiation response functions.

3.1 Radiation Source Modules

The NAIRAS model now incorporates three ionizing radiation sources: the extraterrestrial GCR and SEP sources included in the previous version, and the terrestrial trapped protons (TRP) added in version 3.0. The model components specifying these three radiation sources are described below.

3.1.1 Galactic Cosmic Rays

In the NAIRAS model, GCR ions are propagated from outside the heliosphere to 1 AU (astronomical unit) by solving a steady-state, convective-diffusive transport equation including adiabatic energy loss. A hybrid version of the Badhwar and O'Neill 2010 model (O'Neill, 2010), denoted H-BON10, was developed for NAIRAS to solve GCR heliospheric transport (Mertens et al., 2013). The composition of the GCR gas in the Badhwar and O'Neill model consists of 28 fully ionized nuclear isotopes from hydrogen (Z = 1, A = 1) through nickel (Z = 28, A = 58). The key transport parameter in H-BON10 is the ratio of the diffusion coefficient to the solar wind velocity, in which the time dependence of this ratio is embedded into the so-called solar modulation potential.

The H-BON10 solar modulation potential is parameterized in terms of ground-based neutron monitor count rates obtained from four high-latitude stations which also provide data in real-time. The neutron monitor sites are Thule (77.5ºN, 290.5ºE, R_{vc} = 0.0 GV, where R_{vc} refers to vertical cutoff rigidity), Oulu (65.0ºN, 25.5ºE, R_{vc} = 0.4 GV), Izmiran (55.5ºN, 37.3ºE, R_{vc} = 1.7 GV), and Lomnicky (49.2ºN, 20.2ºE, R_{vc} = 2.8 GV). The solar modulation potential is computed using count rates from the neutron monitor stations via derived linear fit coefficients (Mertens et al., 2013). The solar modulation potential is dependent on the large-scale structure of the interplanetary magnetic field carried by the solar wind. Thus, the fit coefficients between the solar modulation potential and the neutron monitor count rates were derived for three polarity states of the solar polar magnetic field: 1) positive solar cycle (outward directed northern polar field), 2) negative solar cycle (inward directed northern polar field), and 3) transition state (intermediate between positive and negative polarities with high degree of variability). The polarity state of the solar polar magnetic field is determined from field measurements taken by the Wilcox Solar Observatory (WSO) for time periods after 1975. Prior to 1975, the polarity state is determined from sunspot number and the definition of the Hale cycle (Mertens et al., 2013).

Measurements from the satellite-born Payload for Antimatter Exploration and Light-nuclei Astrophysics (PAMELA) experiment was used to derive a temporal-energy dependent correction to the GCR primary proton spectral flux in the H-BON10 model (Adriani et al., 2013). Correction factors were derived for two time periods from a quadratic fit in log-energy to the H-BON10/PAMELA proton spectral flux ratio: 1) a time-period used as a proxy for solar cycle maximum (November 13, 2006 – December 4, 2006), and 2) for a time period at solar cycle minimum (December 6, 2009 – January 1, 2010). The correction factors for the solar cycle

maximum proxy ($r(E,t_{\max})$) and solar cycle minimum ($r(E,t_{\min})$) have the following mathematical form:

$$r(E,t_{\max}) = a_0 + a_1 \ln E + a_2 (\ln E)^2 \quad (1)$$

$$r(E,t_{\min}) = b_0 + b_1 \ln E + b_2 (\ln E)^2 \quad (2)$$

For an arbitrary phase of the solar cycle, the temporal-energy dependent correction factor is computed by a linear weighted average of the two factors in equations (1) and (2), such that

$$r(E,t) = (1 - w(t)) r(E,t_{\min}) + w(t) r(E,t_{\max}), \quad (3)$$

where

$$w(t) = \frac{\Phi(t) - \Phi(t_{\min})}{\Phi(t_{\max}) - \Phi(t_{\min})}. \quad (4)$$

In equation (4), $\Phi(t)$ is the H-BON10 solar modulation potential. PAMELA alpha spectral flux measurements were also analyzed (Adriani et al., 2016). However, no significant differences between PAMELA and H-BON10 alpha spectral flux were found.

The PAMELA-based GCR primary proton spectral flux correction outlined in the previous paragraphs was derived after the initial H-BON10 development reported by Mertens et al. (2013) and prior to the new Badhwar and O'Neill 2020 GCR model (Slaba & Whitman, 2020a), denoted BON2020. A key advantage of the BON2020 model is that the solar modulation potential parameterization is calibrated to all the available GCR flux measurements prior to 2020, including PAMELA data that were not available at the time the GCR primary proton spectral flux correction factor in equation (3) was derived, as well as data from the Alpha Magnetic Spectrometer (AMS-02) onboard the International Space Station (ISS). An important future update to the NAIRAS model is to develop a hybrid version of BON2020, H-BON2020, analogous to the development of H-BON10, that will involve cross correlating the BON2020 solar modulation potential with neutron monitor data so that the BON2020 solar modulation potential can be parameterized in terms of the counts rates from the four high-latitude neutron monitor stations described at the beginning of this section and incorporated into the heliospheric GCR transport module of NAIRAS. Parameterizing the solar modulation potential in terms of the neutron monitor count rates enable the NAIRAS heliospheric GCR transport module to function in both version 3.0 modes of operation: real-time and RoR.

The GCR composition of the H-BON10 model was also expanded to calculate LET spectra out to 100 MeV-cm^2/mg, which is required in the assessment of SEE in the space radiation environment. The highest charge and heaviest nuclear isotope in all versions of the Badhwar and O'Neill model is nickel (Z = 28, A = 58), which can produce a maximum LET of 31.9 MeV-cm^2/mg. As a result, the composition of the H-BON10 model was extended beyond nickel to include the ultra-heavy GCR nuclear isotopes. The highest charge and heaviest isotope included in the expanded H-BON10 GCR model is uranium (Z = 92, A = 238), which can produce a maximum LET of 110.2 MeV-cm^2/mg. The composition of ultra-heavy GCR is based on the relative abundances reported by Mewaldt et al. (1988), which were ultimately based on analysis of measurements taken by the NASA High Energy Astrophysical Observatory (HEAO-3) and Ariel 6 satellite missions (Binns et al., 1982; Fowler et al., 1987). The relative abundances of the H-BON10 GCR composition are shown in Figure 2 as relative fluxes at a kinetic energy insensitive to solar modulation. Figure 3 is an example of the H-BON10 GCR spectral flux.

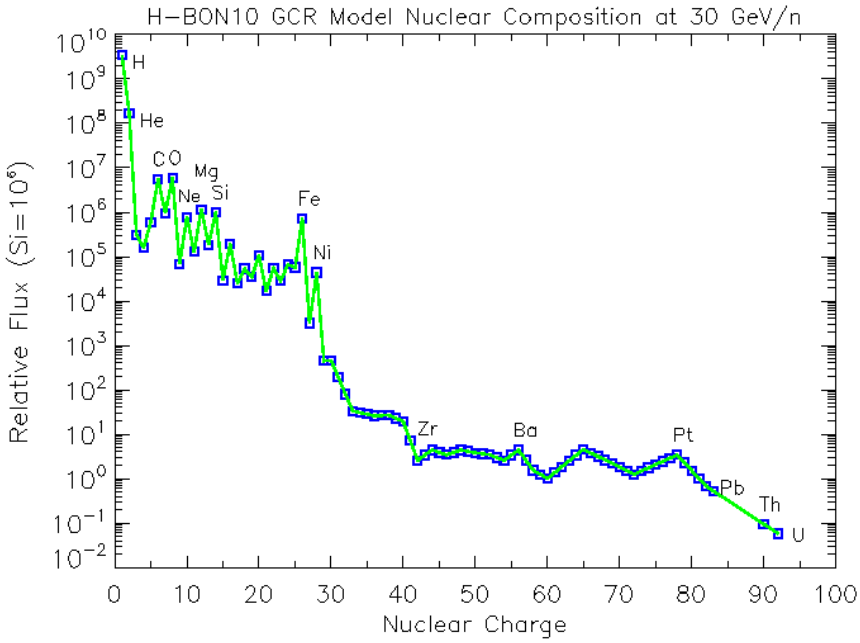

Figure 2: H-BON10 model GCR composition. Relative abundances represented as relative flux at 30 GeV/n, normalized to (silicon) Si = 10^6.

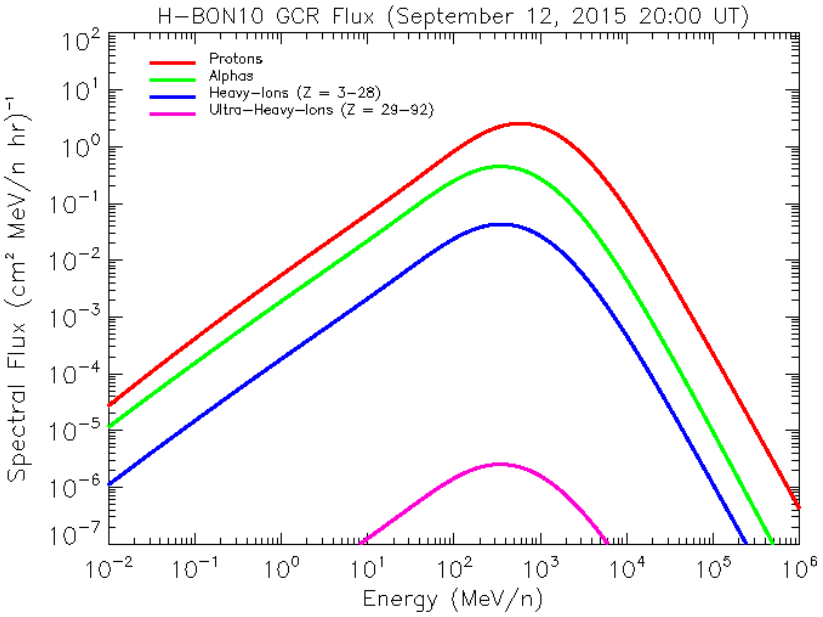

Figure 3: H-BON10 GCR spectral flux computed during the NASA Radiation Dosimetry Experiment (RaD-X) flight campaign.

3.1.2 Solar Energetic Protons

The SEP proton spectrum at 1 AU is determined by a fitting procedure using in-situ measurements of proton flux from the NOAA Geostationary Operational Environmental Satellites (GOES). The spectral fitting algorithm fits analytical representations of the SEP proton

spectrum to either GOES differential proton flux measurements (Mertens et al., 2012, 2010) or GOES integral proton flux measurements, the latter of which is a new feature. The form of the analytical functions is guided by theoretical understanding of the origin, acceleration, and transport of energetic charged particles from their sources in the solar atmosphere through interplanetary space. The analytical forms are: equation (5) single power-law (Tylka & Lee, 2006), equation (6) Ellison-Ramaty (Ellison & Ramaty, 1985), equation (7) Ellison-Ramaty double power-law (Mewaldt et al., 2005; Tylka et al., 2005), sometimes referred to as a Band function, and equation (8) the Weibull distribution (Townsend et al., 2006, 2003; Xapsos et al., 2000), which are expressed as

$$dJ / dE = CE^{-\gamma} \tag{5}$$

$$dJ / dE = CE^{-\gamma} \exp(-E / E_0) \tag{6}$$

$$\begin{aligned} dJ / dE &= CE^{-\gamma_a} \exp(-E / E_0) \text{ for } E \le (\gamma_b - \gamma_a)E_0 \\ &= CE^{-\gamma_b} \left\{ \left[(\gamma_b - \gamma_a)E_0 \right]^{(\gamma_b - \gamma_a)} \exp(\gamma_a - \gamma_b) \right\} \text{ for } E > (\gamma_b - \gamma_a)E_0 \end{aligned} \tag{7}$$

$$dJ / dE = Ck\gamma E^{\gamma - 1} \exp(-kE^{\gamma}), \tag{8}$$

respectively. The spectral (or differential) flux (dJ/dE) is in units of $(cm^2\text{-MeV-s-sr})^{-1}$.

The theoretical interpretations of the analytical spectral forms are the following. The single power-law form in equation (5) represents a diffusive acceleration mechanism for charged particles in a turbulent magnetic field associated with an interplanetary shock (Tylka & Lee, 2006). The constant C is the abundance of a suprathermal seed population injected upstream of the shock, originating from either the solar wind (corona) or flare or both. The power-law index γ characterizes the acceleration in the turbulent magnetic field and is function of the shock compression ratio. The Ellison-Ramaty form in equation (6) has a similar interpretation. The e-folding (or turnover) energy E_0 represents a high-energy limit to the acceleration mechanism, such as escape of the accelerated charged particles from the shock front through spatial diffusion (Ellison & Ramaty, 1985). The double power-law form in equation (7) is a combination of the single power-law and the Ellison-Ramaty forms, which represent two independent sources of seed populations: e.g., a prompt high-energy source at a flare location (single power-law) and a coronal or solar wind source accelerated by a coronal mass ejection (CME) induced interplanetary shock (Mewaldt et al., 2005; Tylka et al., 2005). The Weibull distribution in equation (8) is generally interpreted in statistical theory as a survival probability. An interpretation in terms of physical processes responsible for solar energetic charged particle origin, acceleration, and transport has not been firmly established. In practice, however, this function quite often fits in-situ charged particle flux measurements better than the other spectral forms (Townsend et al., 2006, 2003; Xapsos et al., 2000).

The free parameters for each analytical form of the SEP proton spectrum are derived by a nonlinear, least-square fit to the GOES proton flux measurements. The spectral fitting algorithm uses a Marquardt-Levenberg iteration technique (Brandt, 1999). The analytical function that yields the minimum chi-square residual, among the four functional forms, in the fit to the GOES proton flux measurements, is the selected SEP proton spectrum at 1 AU that is used in the subsequent SEP transport and radiation response function calculations (Mertens et al., 2010, 2012).

A new fitting code was developed in NAIRAS version 3.0 which has the option to fit a SEP proton spectrum to either the differential GOES proton flux channels or the integral proton flux channels. SEP spectral fitting to the GOES differential proton channels has proven to be problematic in practice. The difficulty is encountered at event onset and for weak-to-moderate events due to a combination of high GCR background levels in the high-energy GOES differential proton channels and the energy-dependent arrival times of the SEP protons. Of course, one can always interpolate and extrapolate the GOES differential proton channels. But this approach necessarily requires introducing artificial and subjective criteria in extrapolating beyond the highest energy GOES differential proton channel (~ 600 MeV), which can account for 50% or more of the effective dose in well shielded environments (e.g., aviation altitudes, ISS, Orion MPCV) (cf., Mertens & Slaba, 2019).

Despite the theoretical and practical problems described in the previous paragraphs, the spectral fitting option to the GOES differential proton channels was software hardened to provide physically sensible results when inferring the SEP proton spectrum. One of the software hardening measures implemented was a criterion on the maximum allowed chi-square residual. If the selected spectral form using the algorithm described in this section doesn't meet the absolute goodness criterion of maximum chi-square, then the SEP proton spectrum is determined by log-log interpolation/extrapolation of the GOES differential proton flux measurements, with a hard limit set on the extrapolated flux at high energy. This run option was tested extensively for numerous SEP events, from very weak to extremely large events, and for quiet conditions as well. Inferring a SEP proton spectrum from GOES measurements during quiet time provides a stringent test on the numerical stability of the code. The primary use of this run option is for sensitivity studies and intercomparisons with models that use the GOES differential proton channels to construct the SEP spectrum at 1 AU.

The most important new feature of the NAIRAS version 3.0 SEP spectral fitting code, however, is the option to infer the SEP spectrum from the GOES integral proton flux channels. Because the GOES integral proton flux measurements are well ordered with respect to energy throughout the time evolution of a SEP event – i.e., monotonically decreasing flux with increasing energy – the SEP proton spectrum can be fit to the GOES integral proton channels without artificial assumptions in the extrapolation to high energy. Thus, it is only the physics embodied in the spectral forms in equations (5)-(8) that inform the extrapolation to high energy. Extensive testing of the new NAIRAS SEP spectral fitting algorithm, by fitting to the GOES integral proton channels, has proven the algorithm to be robust against numerical instability and free from erroneous, non-physical fits while simultaneously consistent with the GOES differential proton channel measurements. An example of a spectral fit to GOES integral proton flux is shown in Figure 4 for the January 20, 2005 SEP event, which was also associated with a ground-level enhancement (GLE 69).

Despite the several advantages of SEP spectral fitting using GOES integral flux measurements, this approach is more computationally intensive since numerous improper integrals are evaluated for each GOES integral proton channel and at each iteration step in the inversion algorithm. The temporal fidelity of the NAIRAS RoR flight trajectory predictions needed for government and commercial spaceflight missions and the NOAA Space Weather Prediction Center (SWPC) and the International Civil Aviation Organization (ICAO) goals for aviation radiation nowcasts and forecasts are driving the requirement to predict SEP radiation quantities at 5-minute time intervals. This requirement is difficult to meet using the GOES integral flux measurements to infer the SEP proton spectrum. To circumvent this computational burden, analytical expressions were derived for the Jacobian matrix and vector components of the forward model which are called at each iteration step in the inversion algorithm, based on the

set of four analytical SEP spectral forms in equations (5)-(8) used in the SEP spectral fitting algorithm. This update was successful and enabled the option to fit the SEP proton spectrum to GOES integral flux measurements to be used operationally at 5-minute time intervals. The details of the numerical implementation of the SEP proton spectral fitting algorithm are given in Appendix A.

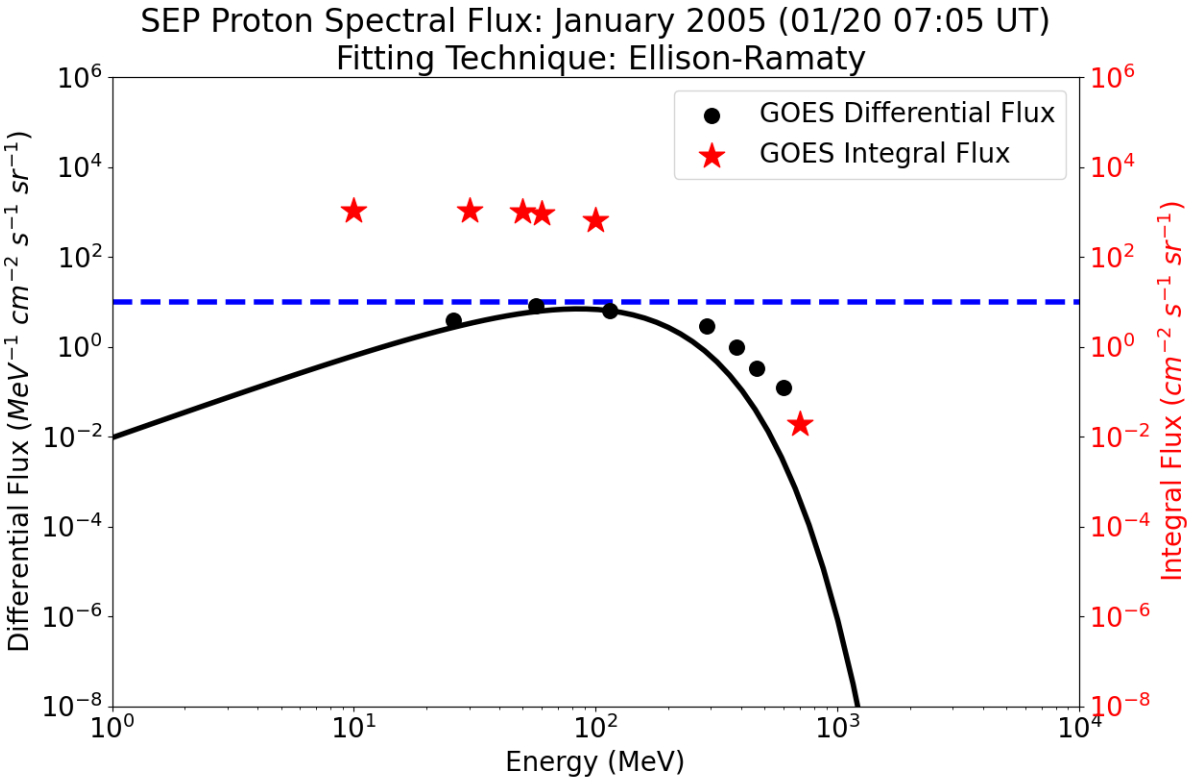

Figure 4: SEP proton spectrum fit (black line) to GOES integral proton flux measurements (red stars). The GOES differential proton flux measurements (black dots) are show as an independent comparison to the inferred spectrum. The horizonal blue line indicates the NOAA/SWPC SEP event threshold in the >10 MeV proton flux channel.

3.1.3 Inner Radiation Belt Trapped Protons

The GEOFFB trapped proton belt model was integrated into NAIRAS version 3.0 to extend the model domain from the atmospheric ionizing radiation environment to the geospace radiation environment (Badavi et al., 2011). GEOFFB is based on the APMIN and APMAX maps of measured trapped proton fluxes at solar minimum (1965) and solar maximum (1970) for solar cycle 20. GEOFFB interpolates/extrapolates beyond the time periods of the APMIN/APMAX proton flux databases using parametric fits derived to account for the long-term drift of the South Atlantic Anomaly (SAA) and the effects of solar cycle modulation on the population of trapped protons in the inner radiation belt.

The solar modulation of the inner belt protons is governed mainly by the cosmic ray albedo neutron decay (CRAND) production mechanism and loss by interactions with the neutral atmosphere (Wilson et al., 2002). Thus, the kinetic rate equation for the trapped proton distribution function (f_p) is approximated by

$$\frac{\partial f_p}{\partial t} \approx P_{\text{CRAND}} - \frac{f_p}{\tau_{\text{atm}}} \ , \tag{9}$$

where P_{CRAND} is the CRAND production rate and τ_{atm} is the atmospheric loss time constant. Under steady-state conditions, the trapped proton distribution function is proportional to the product of the CRAND production rate and atmospheric loss time constant, such that

$$f_p \sim P_{\text{CRAND}} * \tau_{\text{atm}} . \tag{10}$$

Therefore, the strength and temporal variation of the solar cycle modulation of the trapped protons is parameterized in GEOFFB by a variable that is the product of neutron monitor count rate and the F10.7 index (Badavi et al., 2011). The rate of secondary atmospheric neutrons detected by ground-based neutron monitors is a proxy for the CRAND production mechanism and its variation with solar cycle. The solar radio emission F10.7 index and its solar cycle variation is a proxy for atmospheric loss of trapped protons and the solar cycle modulation of this loss mechanism due to the upper atmospheric neutral density.

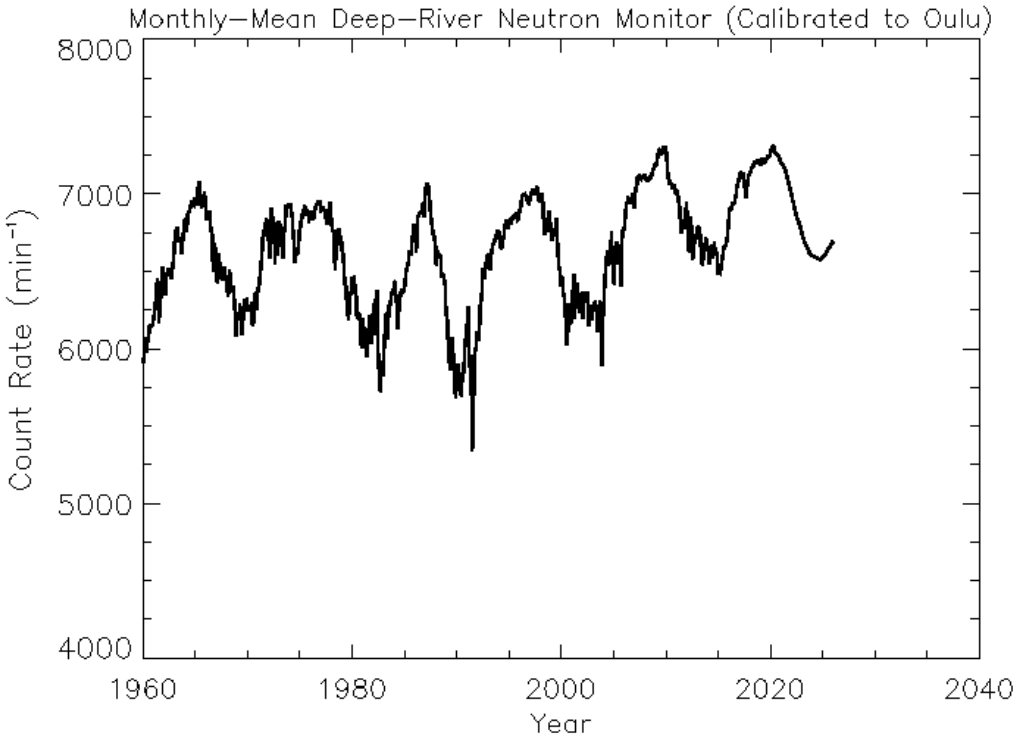

Figure 5: Deep-River neutron monitor (DRNM) monthly averaged count rates. After 1995 Oulu neutron monitor data, normalized to DRNM over the period of data overlap (1965-1995), are used to continue DRNM data.

The parameterization of the solar cycle modulation function, and the parameterization of the long-term drift of the SAA, were calibrated against extensive onboard measurements from the ISS and the Space Transportation System (STS: Shuttle) (Badavi et al., 2011). This approach successfully accounts for solar cycle modulation of the inner belt trapped protons while eliminating unrealistic extrapolations produced by simply incorporating the secular changes in the internal geomagnetic field model (Heynderickx, et al., 1996). Nevertheless, these

parameterizations were derived from spaceflight measurements at altitudes less than 500 km. An important next step in the NAIRAS version 3.0 development is to conduct extensive spaceflight validation studies at altitudes above ISS, to assess the GEOFFB model uncertainty at higher altitudes and better identify the missing physics needed to improve the model.

The key data inputs that parameterize the solar cycle modulation in the GEOFFB trapped proton model are shown in Figures 5 and 6. Deep-River neutron monitor data (DRNM) were used initially in the development of the solar cycle modulation. DRNM was discontinued in 1995. A normalization factor was determined between DRNM and Oulu neutron monitor data over the period of data overlap (1965-1995), and normalized Oulu data have been used as a DRNM proxy to continue the DRNM count rates in the GEOFFB model from 1995 to the present (Wilson et al., 2002). DRNM monthly data from 1960 to 2025 are shown in Figure 5. The data in Figure 5 were extrapolated from year 2020 to 2025 by correlating DRNM to sunspot number (SSN) and using the SSN forecasts provided by NASA Marshall Space Flight Center (MSFC) (https://www.nasa.gov/msfcsolar/datasources). The SSN data were version 2.0, 13-month smoothed data from the Royal Observatory in Belgium (https://wwwbis.sidc.be/silso/datafiles). The SSN forecasts were 50% percentile projections which were also based on SSN version 2.0. The 10.7 cm solar radio emission (F10.7) index data are shown in Figure 6, which were obtained from NASA Goddard Space Flight Center OMNIWeb (https://omniweb.gsfc.nasa.gov/form/dx1.htm). The F10.7 data were also extrapolated from 2020 to 2025 using 50% percentile projection forecasts from NASA MSFC.

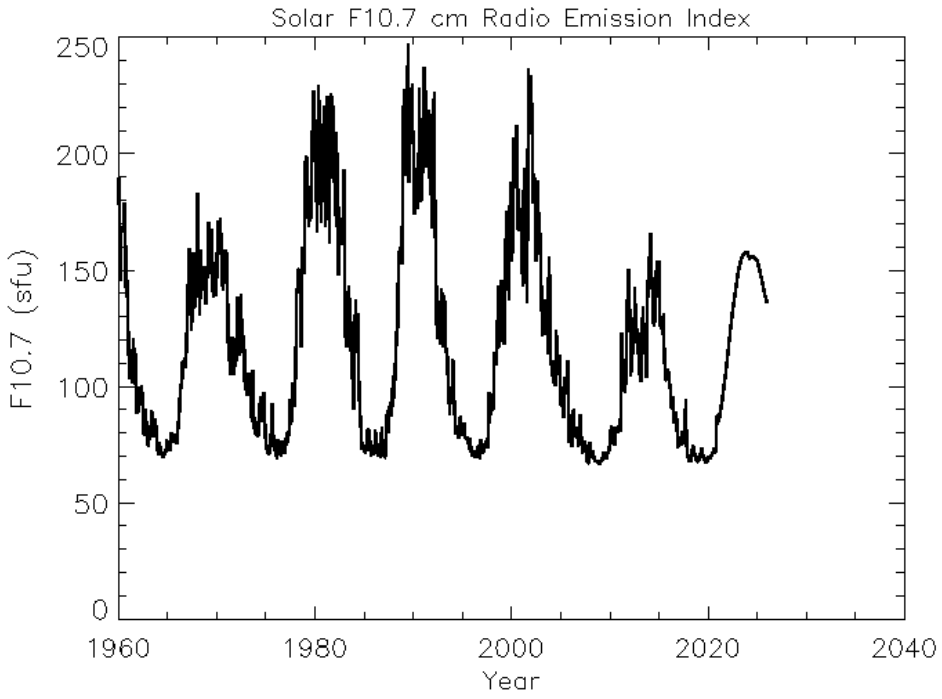

Figure 6: Monthly averaged solar radio emission 10.7 cm (F10.7) index. The F10.7 data are reported in solar flux units (sfu: 10^{-22} m^{-2} Hz^{-1}).

To provide rapid post-flight analysis, the NAIRAS RoR run option was developed so that this service can be utilized within hours after the launch of a spacecraft. The GEOFFB solar cycle modulation parameterization, however, is based on the prior 15-month average (current month

inclusive) of the DRNM and F10.7 data. This fact is the reason these two parameters are extrapolated using the solar cycle forecasts of these quantities, as described in this paragraph. The maximum monthly error in the solar cycle modulation correction over the period 2021-2022 is around 20%. To ensure the extrapolation error does not become too large, a future improvement to the implementation of GEOFFB in NAIRAS version 3.0 will be to update the DRNM and F10.7 data monthly and rescale the remaining forecast period. The result of this step will be that the current DRNM count rate and F10.7 index are based on a 1-month extrapolation at most.

An example trapped proton spectrum from GEOFFB is presented in Figure 7 for November 2, 2003. The spectrum is shown for a geographic location near the central region of the SAA. The altitude of the spectrum is in the range of ISS altitudes. The flux of trapped protons at this geographic coordinate remains high from low energies to 100 MeV and diminishes rapidly by 500 MeV and greater.

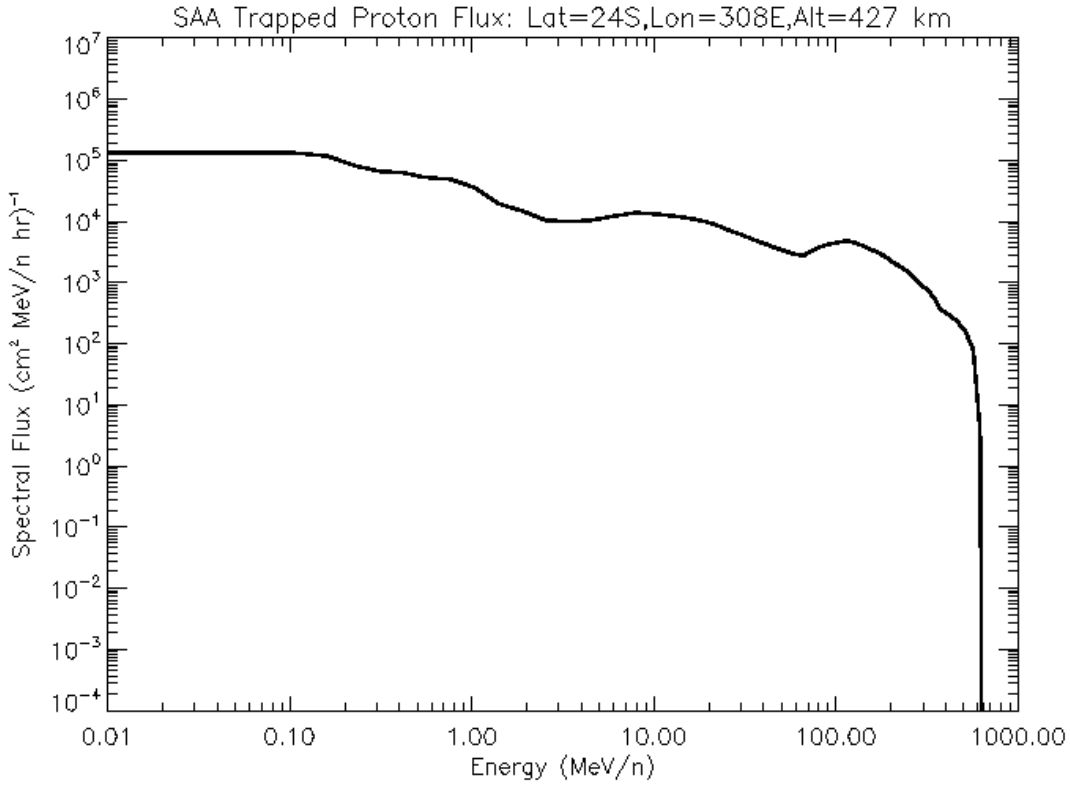

Figure 7: Trapped proton spectral flux from the GEOFFB model at a geographic location near the central region of the SAA and at an altitude in the range of ISS altitudes.

3.2 Geomagnetic Transmission

The geomagnetic field (internal field plus magnetospheric contributions) provides a form of momentum shielding, or attenuation, with respect to charged particles incident on the geospace environment, such as the GCR and SEP ions (Mertens et al., 2012). The incoming charged particles are deflected by the geomagnetic field via the Lorentz force and lower momentum

particles can be deflected back out to space or towards the Earth's surface or confined to quasi-trapped orbits. This spectral filtering is quantified by the cutoff rigidity. Rigidity is defined as the particle's momentum per charge. At each geographic location (latitude, longitude, altitude), there is a cutoff rigidity for each arrival direction (zenith and azimuth angles) of incoming charged particle such that the charged particle must have a rigidity greater than or equal to the cutoff rigidity to reach that location. Once the cutoff rigidity is known, the minimum access energy of any particle of charge number Z and mass number A can be determined from the relativistic energy equation (Mertens et al., 2010, 2012).

The solution of charged particle motion in a pure dipole magnetic field was examined by Stormer (1965). The azimuthal angular momentum is conserved because of the symmetry of the dipole field (Stormer, 1965; Van Allen, 1968). This allows the directional cutoff rigidity to be derived analytically, which can be expressed in the following form

$$R_{dc}(r,\psi,\varphi;\varepsilon,\beta) = \left(\frac{r_{ref}}{r}\right)^2 \frac{4R_{vc}(r_{ref},\psi,\varphi)}{\left[1+\sqrt{1-\sin\varepsilon\sin\beta\cos^3\psi}\right]^2} \ . \tag{11}$$

In equation (11), the radial distance, magnetic latitude, and magnetic longitude are denoted r, ψ, and ϕ, respectively. The zenith direction of the arriving charged particle with respect to the local vertical direction is denoted ε, while β corresponds to the azimuthal direction of the arriving charged particle with respect to the local north direction, and clockwise rotation from local north denotes a positive azimuth angle (Smart & Shea, 2005). The cutoff rigidity for vertically arriving particles, or vertical cutoff rigidity, is denoted R_{vc}, which is calculated at a reference altitude r_{ref}.

The Earth's magnetic field, however, is not a pure dipole. The internal magnetic field consists of dipolar and non-dipolar contributions. Furthermore, the dipole moment is off-center and tilted with respect to the Earth's rotational axis. The magnetospheric current systems generate their own magnetic fields which combine vectorially with the internal magnetic field. Thus, the complexities of the actual geomagnetic field require numerical methods to determine the cutoff rigidity (Mertens et al., 2012). The numerical solution, however, is computationally time-consuming. The approach in NAIRAS version 3.0 is to employ a numerical model to calculate the vertical cutoff rigidity and use the analytical Stormer equation in equation (11) to scale the numerically-determined vertical cutoff rigidity to other arrival directions.

The NAIRAS geomagnetic vertical cutoff rigidity model is based on the CISM-Dartmouth model developed by Kress et al. (2004, 2010). The CISM-Dartmouth model calculates the vertical cutoff rigidity from numerical solutions of charged particle trajectories in a dynamically varying geomagnetic field that includes both the internal magnetic field and the magnetospheric magnetic field contributions (Mertens et al., 2012). The internal magnetic field model is the International Geomagnetic Reference Field (IGRF) model (Mertens et al., 2012). The magnetospheric magnetic field model is the semi-physics-based TS05 model (Tsyganenko & Sitnov, 2005). The main input data to the TS05 model are the solar wind plasma parameters and interplanetary magnetic field (IMF) components, which are obtained from NASA Advanced Composition Explorer (ACE) satellite, or NOAA Deep Space Climate Observatory (DSCOVR) satellite, and the SYM-H or Kyoto Dst index. The CISM-Dartmouth model employs numerical procedures that provide reasonably accurate vertical cutoff calculations while also enabling the cutoffs to be calculated globally in real-time (Kress et al., 2010; Mertens et al., 2010). The

CISM-Dartmouth vertical cutoff model has been a component of the NAIRAS model from its inception.

Several extensions and updates to the CISM-Dartmouth cutoff model have been made in the development of NAIRAS version 3.0, which were motivated mostly by the development of the RoR capability. The cutoff model now includes an option to use the T89 magnetospheric magnetic field model (Tsyganenko, 1989), which uses only the Kp-index as the input quantity to capture the dynamical response to solar-geomagnetic variability. The T89 model does not represent the response of the magnetosphere to geomagnetic variably nearly as well as the TS05 model (see Figure 8), but prior to the real-time operation of the ACE satellite in 1995, there was no better representation of the magnetospheric magnetic field. The T89 option allows historical solar-geomagnetic storm events to be analyzed prior to 1995.

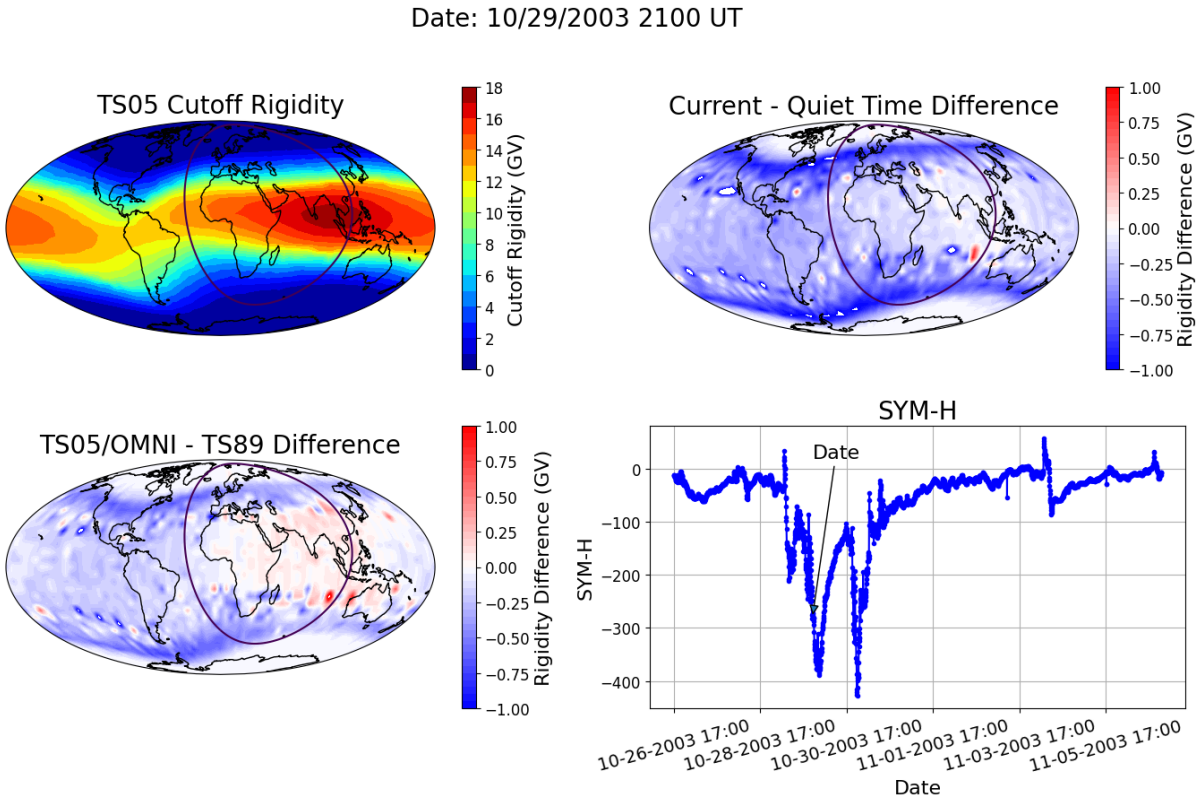

Figure 8: Vertical geomagnetic cutoff rigidity model calculations at 20 km for aviation radiation applications. The time period shown is during the maximum suppression of the cutoff for the Halloween 2003 solar-geomagnetic storm events. Top left: vertical cutoff using TS05 magnetospheric magnetic field model. Top right: cutoff differences between the geomagnetic storm and quiet-time period before the geomagnetic activity. Bottom left: cutoff differences between TS05 and T89 field models. Bottom right: SYM-H index. The arrow points to the time of maximum cutoff rigidity suppression. The circle in the cutoff panels encompasses the daytime region for 21:00 UT on October 29, 2003.

Supporting software was developed to maintain the databases of the input solar-geomagnetic parameters required by the TS05 and T89 models. The archived ACE real-time 5-minute solar wind data products have large data gaps during SEP events. A data gap filling algorithm was developed and automated to pull from other sources to fill in the missing ACE solar wind data during SEP events. In addition, the input interface of the CISM-Dartmouth cutoff

model was modified to allow the selection of global cutoff calculations or cutoff calculations at discrete geographic locations, significantly reducing the computational time for the RoR flight trajectory run option. The cutoff code was also modified to provide greater flexibility and efficiency in parallelizing the vertical cutoff calculations for both the NAIRAS version 3 global and flight trajectory run options (see Table 1).

Moreover, in the geospace environment the vertical cutoff rigidity alone is not adequate to parameterize the geomagnetic transmission of GCR and SEP primary particle spectra through the magnetosphere, which is a customary approximation for the atmospheric ionizing radiation environment. Thus, the version 3.0 NAIRAS model was updated to include altitude-dependent and rigidity-dependent geomagnetic transmission function calculations.

The transport of free-space GCR and SEP ions through the magnetosphere can be described in terms of the geomagnetic transmission function such that

$$\Phi_i(\mathbf{r},\mathbf{\Omega},R) = \int_{\mathbf{\Omega}'}\int_0^\infty T(\mathbf{r};\mathbf{\Omega},R;\mathbf{\Omega}',R')J_i(\mathbf{\Omega}',R')d\mathbf{\Omega}'dR' \quad . \tag{12}$$

In equation (12), $\Phi_i(\mathbf{r},\mathbf{\Omega},R)$ is the directional-differential flux of GCR or SEP particle type i at location $\mathbf{r}$ moving in direction $\mathbf{\Omega}$ with rigidity R; $J_i(\mathbf{\Omega},R)$ is the free-space, directional-differential flux of GCR or SEP particle type i outside the magnetosphere at 1 AU.

The geomagnetic transmission function is independent of particle type in rigidity space and is approximated by the functional form

$$T(\mathbf{r};\mathbf{\Omega},R;\mathbf{\Omega}',R') = H[R' - R_{dc}(\mathbf{r},\mathbf{\Omega}')]\delta(R - R') \tag{13}$$

where $H(x)$ is the Heavyside step function defined by $H(x) = 1$ if $x > 1$; otherwise, $H(x) = 0$. The Dirac delta function in rigidity implies the assumption that there are no energy changing processes in the transport through the magnetosphere. The directional cutoff rigidity $R_{dc}(\mathbf{r},\mathbf{\Omega})$ is given by equation (11). The free-space GCR or SEP directional-differential flux is assumed to be directionally isotropic. Given these assumption and by substituting equation (13) into equation (12), the magnetospheric transport equation in equation (12) is then approximated by

$$\Phi_i(\mathbf{r},\mathbf{\Omega},R) \approx \overline{T}(\mathbf{r},R)J_i(R) \tag{14}$$

where $J_i(R)$ is the free-space, omni-directional GCR or SEP differential flux of particle type i. The directional-integrated geomagnetic transmission function in equation (14) is given by

$$\overline{T}(\mathbf{r},R) = \int_{\mathbf{\Omega}'} H[R - R_{dc}(R,\mathbf{\Omega}')]d\mathbf{\Omega}' \tag{15}$$

where the integration over solid angle in equation (15) includes the Earth's shadow.

An example of NAIRAS version 3.0 magnetospheric transport is shown in Figures 9 and 10. The geomagnetic transmission function at an altitude in the LEO radiation environment is shown in Figure 9. The vertical dashed line denotes the vertical geomagnetic cutoff rigidity for this location. The effect of the altitude and rigidity dependences of the geomagnetic transmission function is that a unique, single value of the cutoff rigidity cannot be defined. The upper bound of the geomagnetic transmission function at high rigidity is not unity due to the Earth's shadow effect. The GCR differential flux at a location in the LEO radiation environment, after magnetospheric transport of the free-space GCR, is shown in Figure 10.

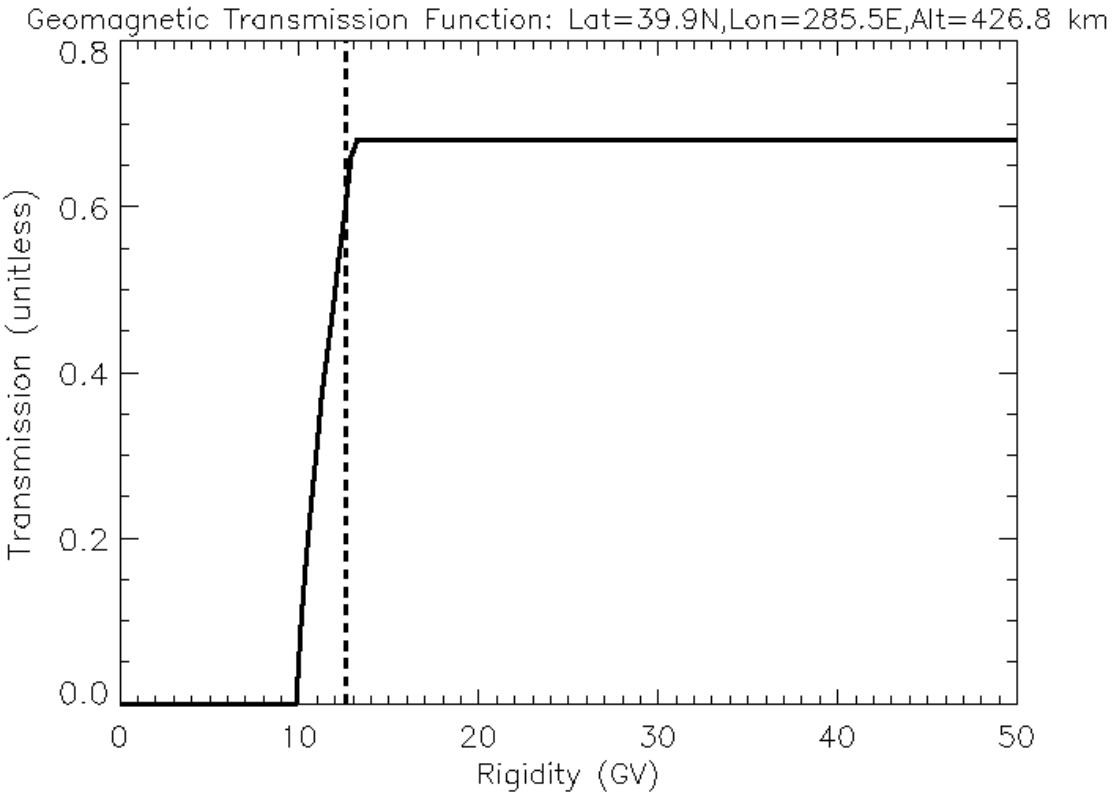

Figure 9: Geomagnetic transmission function at an altitude in the LEO radiation environment. The vertical dashed line denotes the vertical cutoff rigidity.

3.3 Material Radiation Transport

The transport of ionizing radiation through the atmosphere and aircraft or spacecraft vehicle shielding is calculated using the HZETRN2015 deterministic transport code (Slaba and Stoffle, 2017; and references therein). HZETRN numerically solves the time-independent, coupled, linear Boltzmann transport equations. The transport interaction processes include energy slowing down of the incident projectile and fragmentation ions through ionization and atomic excitation of the material medium, nuclear scattering and attenuation, and the production of secondary particles from nuclear reactions between the projectile ions and the material of the target medium (Mertens et al., 2012). Heavy-ions, pions, muons, and electromagnetic cascade particles are treated within the straight-ahead approximation (Slaba et al., 2013a, 2013b). Neutrons and light-ion transport utilize a bi-directional transport approach which incorporates albedo neutron contributions (Slaba et al., 2010).

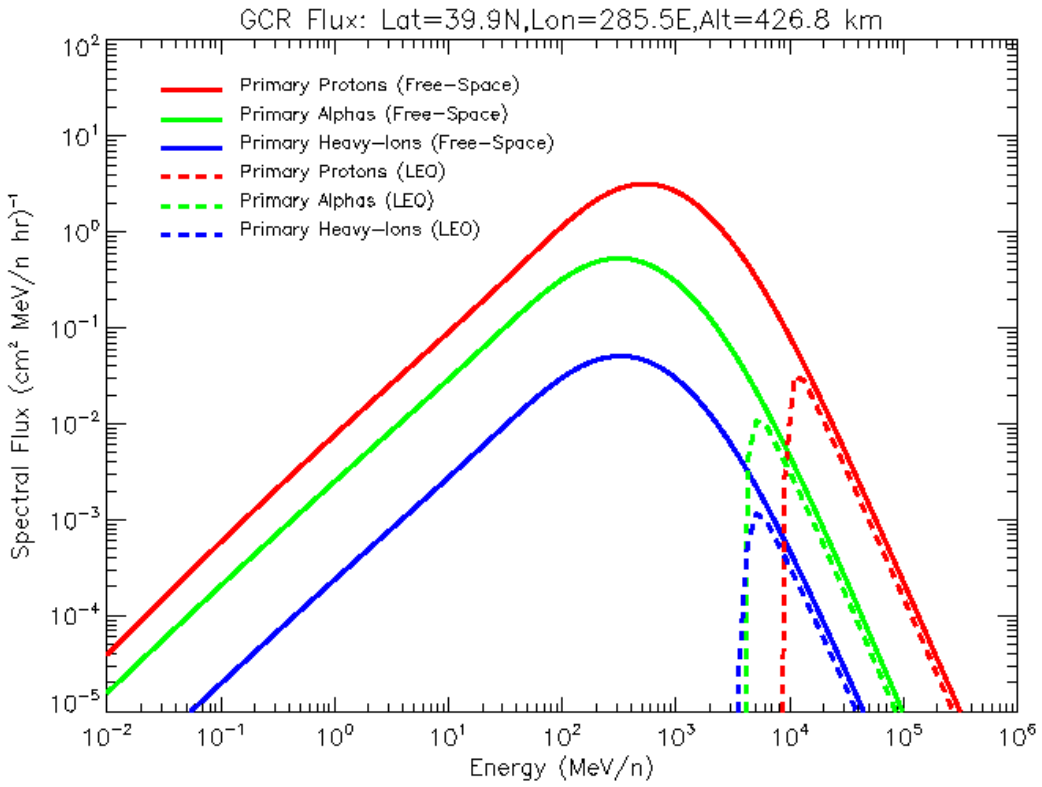

Figure 10: Free-space GCR spectral flux transported through the magnetosphere to an altitude in the LEO radiation environment via the geomagnetic transmission function (see Figure 9). Heavy-ion GCR spectral flux is a sum of GCR spectra for all ions with charge and mass number greater than helium.

In the previous version of NAIRAS, HZETRN solved coupled transport equations for 59 isotopes to calculate the radiation response functions along each ray direction from the GCR primary source ions. In NAIRAS version 3.0, the expanded GCR composition described in section 3.1.1 to calculate LET spectra out to 100 MeV-cm^2/mg requires the solution of 116 coupled transport equations along each ray direction. The pre-computed atomic and nuclear databases utilized by HZETRN were updated to include the ultra-heavy GCR nuclear isotopes in the GCR transport.

The atmospheric ionizing radiation transport in the previous version of NAIRAS implemented a transport scheme along the vertical direction with the GCR or SEP differential flux at the top boundary of the neutral atmosphere approximated by a projection of the directionally isotropic GCR and SEP source differential flux along the vertical direction (Mertens et al., 2013). Measurements taken by the NASA Radiation Dosimetry Experiment (RaD-X) balloon flight showed that transport along a single direction in the atmosphere is insufficient at predicting dosimetric quantities at high-altitudes above the commercial aviation radiation environment (Norman et al., 2016). To better characterize the radiation environment of a spaceflight over the entire mission, from launch to orbit and return, the atmospheric transport in NAIRAS version 3.0

was updated to include multi-directional transport through the atmosphere. The number of ray directions were optimized by comparing model calculations with RaD-X dosimetric measurements (Mertens et al., 2016b).

The NAIRAS version 3.0 multi-directional atmospheric ionizing radiation transport approach can be summarized in terms of the directional-integrated flux. This quantity is required to compute the dosimetric quantities (Mertens et al., 2012, 2013) and the new output flux and fluence quantities listed in Table 1 for assessing SEE. In the atmosphere, assuming azimuthal symmetry, the directional-integrated flux for particle type i can be approximated by

$$\phi_i(\mathbf{r},E) = \int \Phi_i(\mathbf{r},\mathbf{\Omega},E)d\mathbf{\Omega} \approx 2\pi\left[\frac{1}{N}\sum_j \Phi_i(\mathbf{r},u_j,E)\right], \tag{16}$$

where $u_j = \cos\varepsilon_j$ and ε_j is the zenith angle along ray direction j. The integral over zenith direction is discretized into a sum over equal segments in $\cos\varepsilon$. Thus, for N ray directions $\Delta u = 1/N$ such that

$$\cos\varepsilon_{j+1} = \cos\varepsilon_j - \frac{1}{N} \tag{17}$$

and $\cos\varepsilon_1 = 1$ for the vertical direction. For a given number of ray directions, N, the radiation transport equations are solved along each ray direction given by the zenith angles computed from equation (17). At each altitude in the atmosphere, the differential fluxes along these rays directions are averaged, and including the 2π scale factor, to obtain the directional-integrated flux in equation (16).

The fundamental spatial coordinate in ionizing radiation transport is the areal depth in the material medium, in units of g/cm^2 (Mertens et al., 2012). For atmospheric transport in NAIRAS version 3.0, the depth at each altitude and ray direction in equation (16) is computed from the U.S. Standard Atmosphere (U.S. Standard Atmosphere, 1976). The thermodynamic variables of the U.S. Standard Atmosphere are shown in Figure 11. Within each altitude layer of the U.S. Standard Atmosphere, the pressure is assumed to vary exponentially, the temperature is assumed to vary linearly, and the density is determined from temperature and pressure at the layer boundary by the ideal gas law in the calculation of atmospheric depth. The atmospheric density is given by

$$\rho(z) = C_1 \frac{P(z)}{r_a T(z)} \tag{18}$$

where $C_1 = 10^{-4}$ is a conversion factor so that the density, ρ, is in units of g/cm^3, pressure, P, in mbar, and temperature, T, in units of Kelvin. The specific gas constant of air, r_a, is 0.28706 J/K/g. The atmospheric depth at the top of the U.S. Standard Atmosphere is approximated (z_{top}) by

$$d(z_{top}) = C_2 \rho(z_{top}) H(z_{top}) \ , \tag{19}$$

where H is the atmospheric scale height defined as

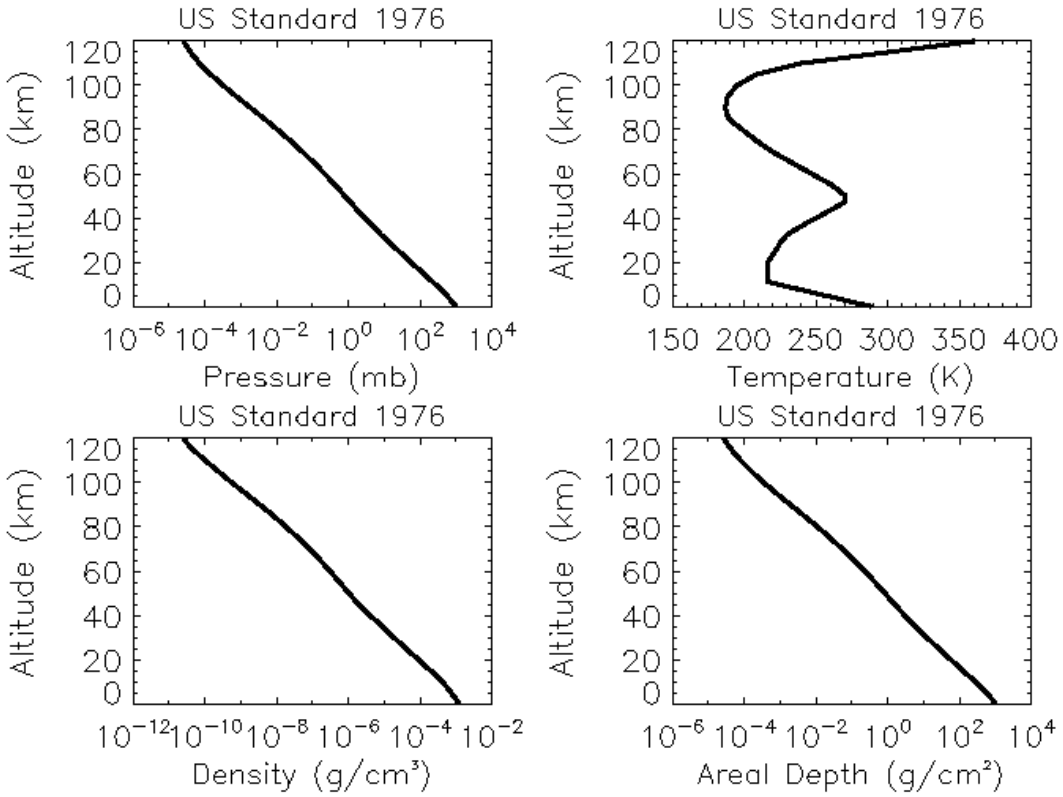

Figure 11: U.S. Standard Atmosphere thermodynamic variables. The areal depth was computed from the pressure, density, and temperature as described in the text.

$$H(z) = \frac{r_a T(z)}{g}, \tag{20}$$

and g is the gravitational acceleration 9.80665 m/s^2. The conversion factor $C_2 = 10^5$ in equation (19) ensures the depth is in units of g/cm^2. Given the depth at the top of the atmosphere in equation (19), the depth at altitude z_N in the U.S. Standard Atmosphere is approximated by the sum of increments of depth for each subsequent vertical layer, such that

$$d(z_N) = \sum_{i=2}^{N} \Delta d(z_i) + d(z_{top}) \tag{21}$$

where the increment in depth from an atmospheric layer is computed explicitly by

$$\Delta d(z_i) = \int_{z_i}^{z_{i-1}} \rho(z) dz \tag{22}$$

and $z_{i-1} > z_i$.

Given the variation in the thermodynamic variables described is this section, the following expression for the incremental depth is derived

$$\Delta d(z_i) = C_2 \frac{\rho(z_{i-1})(z_{i-1} - z_i)}{\gamma\left[1 - \left(T(z_i)/T(z_{i-1})\right)\right]}\left[\left(\frac{T(z_i)}{T(z_{i-1})}\right)^{-\gamma} - 1\right], \tag{23}$$

where

$$\gamma = \frac{z_{i-1} - z_i}{H(z_{i-1}) - H(z_i)}. \tag{24}$$

Notice that equation (23) becomes ill-defined in isothermal regions of the atmosphere. In the U.S. Standard Atmosphere shown in Figure 11, the isothermal regions are near the tropopause and stratopause. The following expression is derived for the incremental depth of an isothermal atmospheric layer

$$\Delta d(z_i) = C_2 \rho(z_{i-1}) H(z_{i-1})\left[\exp\left(\frac{z_{i-1} - z_i}{H(z_{i-1})}\right) - 1\right]. \tag{25}$$

The expressions for the atmospheric depth, equation (23) and equation (25), were derived for vertical layers, or equivalently, for zenith angle equal to zero, $\varepsilon = 0$. For off-vertical ray directions, as is needed in computing the directional-integrated flux in equation (16), the layer thicknesses, $z_{i-1} - z_i$, in equations (23)-(25) are replaced by the layer slant path thickness Δs_i, which can be derived from geometry and given by

$$\Delta s_i^2 = (\mathrm{Re} + z_i)^2 + (\mathrm{Re} + z_{i-1})^2 - 2(\mathrm{Re} + z_i)(\mathrm{Re} + z_{i-1})\cos\left(\varepsilon - \eta\right), \tag{26}$$

where

$$\sin\eta = \sin\varepsilon\left(\frac{\mathrm{Re} + z_i}{\mathrm{Re} + z_{i-1}}\right). \tag{27}$$

and Re is the average Earth radius (6371.2 km).

The multi-directional atmospheric ionizing radiation transport approach described is this section made a significant improvement in predicting the dosimetric quantities at altitudes above the commercial aviation radiation environment. A comparison between the NAIRAS model predictions of absorbed dose rate and corresponding measurements taken during the RaD-X high-altitude balloon flight is shown in Figure 12 (Mertens et al., 2016b). The NAIRAS version 3.0 model calculations of absorbed dose rate in tissue agree with the tissue-equivalent proportional counter (TEPC) instrument to within ~8% in RaD-X science region A (21-27 km) and within ~15% in region B (> 32.5 km). The RaD-X campaign consisted of a high-altitude balloon flight, NASA ER-2 and Cessa Conquest II aircraft flights, and coordinated aircraft measurements taken onboard a commercial Lufthansa flight (Mertens et al., 2016b). The RaD-X campaign flight measurements included absorbed dose in silicon, absorbed dose in tissue, dose equivalent, and ambient dose equivalent covering seven altitude regions from 0-40 km. Extensive NAIRAS/RaD-X comparisons showed that six ray directions, $N = 6$, provide sufficient accuracy in the multi-directional atmospheric ionizing radiation transport procedure to maintain the NAIRAS model dosimetric predictions to within 30% of the RaD-X flight measurements, which is within measurement uncertainty. The details of the NAIRAS/RaD-X validation study will be reported in a future publication.

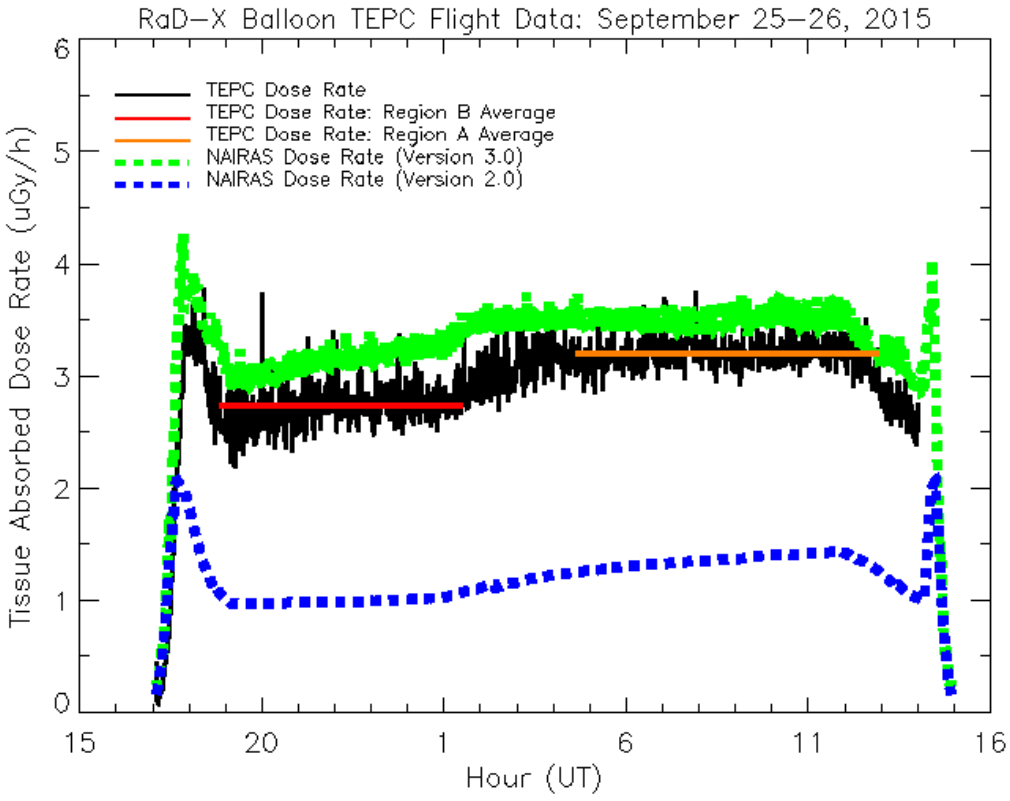

Figure 12: Comparison of NAIRAS predictions of absorbed dose rates in tissue with TEPC measurements taken during the NASA RaD-X high-altitude balloon flight.

4.0 NAIRAS Model RoR Output

Presented in this section are new NAIRAS version 3.0 results with emphasis on the extension of the model domain to the geospace and free-space radiation environments. Examples of the dosimetric and new radiative flux and fluence quantities at a LEO altitude and for the actual ISS trajectory are shown in section 4.1. Dose comparisons between NAIRAS predictions and NASA EFT-1 flight measurements at MEO are presented in section 4.2. Preliminary results of NAIRAS predictions in cislunar orbit during the recent NASA Artemis 1 flight mission are shown in section 4.3.

4.1 Low-Earth Orbit

A LEO flight trajectory comparable to the early ISS orbit was constructed to benchmark the new features of NAIRAS version 3.0, especially the extension of the model from the atmosphere to the geospace environment. The example flight trajectory has an orbital inclination of 51.6º and an altitude of 450 km. The datetime of the trajectory is the 24-hour period from November 2, 2003 16:00 UT to November 3, 2003 16:00 UT. This time period is during the Halloween 2003 SEP events and includes GLE 67 and a geomagnetic storm for testing a wide range of space weather phenomena in the NAIRAS RoR flight trajectory run option. The flight trajectory as a function of geographic latitude and longitude for the 24-hour period is shown in Figure 13. The trajectory points have a uniform 1-minute time resolution.

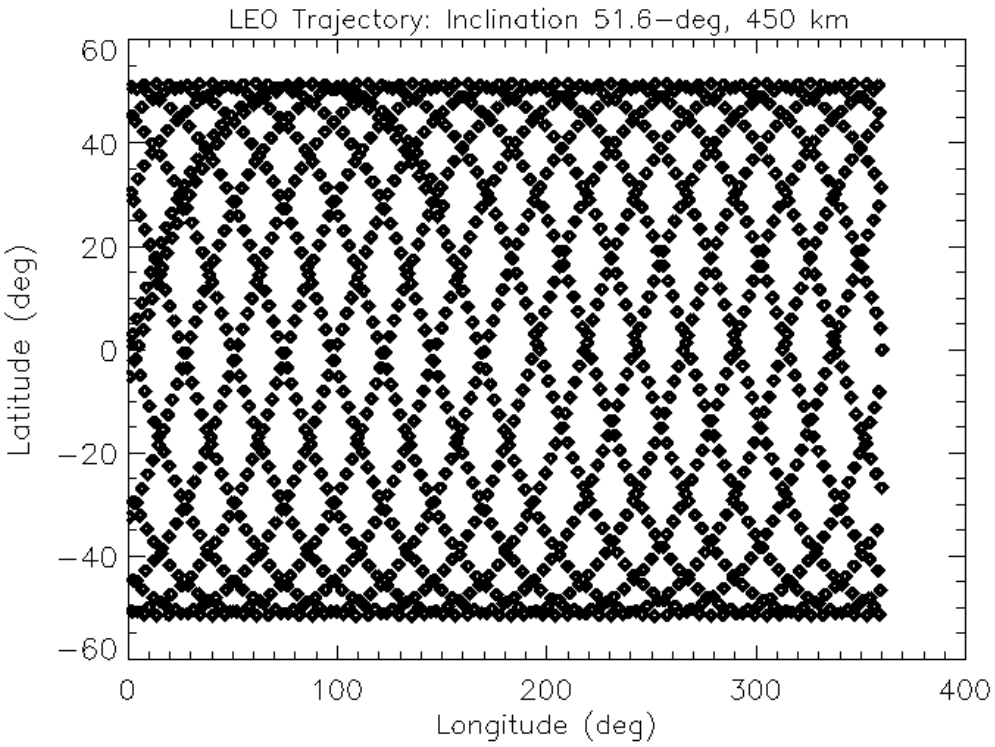

Figure 13: Example LEO flight trajectory points used to test the new NAIRAS version 3.0 output products for the RoR flight trajectory run option. The figure shows the trajectory points for a 24-hour period with uniform 1-minute temporal resolution.

The effective dose rates for the example LEO flight trajectory are shown in Figure 14. A fictitious launch phase for the trajectory was added at the beginning of the example flight to test the new atmospheric ionizing radiation transport procedures discussed in section 3.3. This launch phase can be seen in the effective GCR dose rates in Figure 14. The example LEO flight trajectory passes through the SAA five times in the 24-hour period and crosses the edge of the SAA near the end of the orbit period, which is evident in the effective dose rates from the trapped protons. The SEP dose is also evident at the highest latitude points along the trajectory. The dose rates were calculated for a spacecraft shielding of 50 g/cm^2 aluminum, which is consistent with the median aluminum-equivalent shielding distributions surrounding radiation detectors on ISS (Badavi et al., 2011; Slaba et al., 2020b). The time-integrated flight effective dose for the 24-hour period for the GCR and TRP sources are 235 uSv and 153 uSv, respectively, with a GCR + TRP combined total of 388 uSv. The NAIRAS model results in Figure 14 are for one day in the downward side of solar cycle 23, which included a recovering Forbush decrease during GLE 69 (Mertens et al., 2010, 2012). Nevertheless, these results are consistent with solar cycle averaged daily total effective dose of 438 uSv reported by Cucinotta et al. (2008), and the GCR and TRP daily effective doses of 233 uSv and 166 uSv, respectively, near solar cycle minimum reported by Wu et al. (1996). The total SEP effective dose computed by NAIRAS for this 24-hour period is 19 uSv.

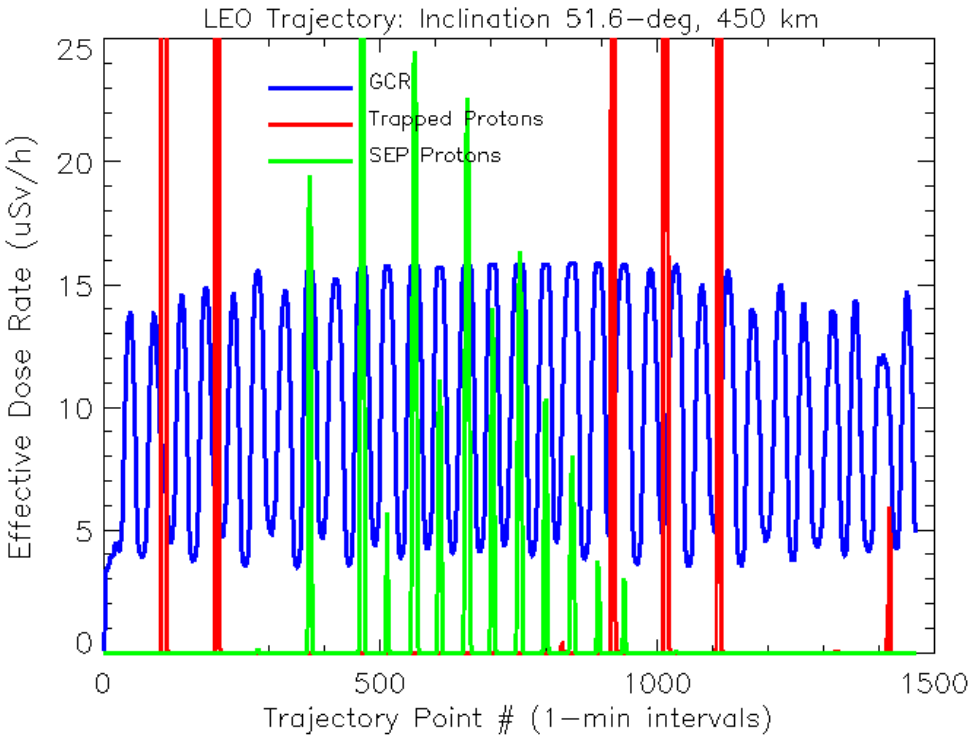

Figure 14: NAIRAS version 3.0 calculations of effective dose rates for the LEO flight trajectory shown in Figure 13. The datetime of the trajectory at the altitude of 450 km is the 24-hour period from November 2, 2003 16:00 UT to November 3, 2003 16:00 UT. A fictitious launch phase was added to the beginning of this example flight. The spacecraft shielding is 50 g/cm^2 aluminum

Vertical cutoffs shown in Figure 15 at the example flight trajectory points in Figure 13 are computed in two ways: 1) using just the internal magnetic field of the Earth (IGRF), and 2) the internal magnetic field plus the magnetospheric magnetic field contributions using the TS05 model (IGRF + TS05). Recall from section 3.2 that the spectral filtering of GCR and SEP ions by the geomagnetic field is a function of the vertical cutoff rigidity. The time period for the cutoff calculations is the same as for the effective dose rates shown in Figure 14. During this time, the geospace environment is recovering from the enhanced geomagnetic activity from the Halloween 2003 storm events. The effect of geomagnetic storm activity is to suppress the cutoff rigidity (Kress et al., 2010; Mertens et al., 2010), which in turn increases the GCR and SEP dosimetric and flux and fluence quantities. The cutoff rigidity suppression is greatest at high latitudes. All the NAIRAS version 3.0 output products presented in this section are based on including the dynamical response of the geomagnetic field by computing vertical cutoff rigidities using the internal field plus the TS05 magnetospheric magnetic field model, as described in section 3.2.

The next three figures are examples of NAIRAS version 3.0 differential and integral flux and fluence quantities that are used in radiation effects models to assess SEE. GCR integral LET flux is shown in Figure 16 for the flight trajectory shown in Figure 13. The user-input, threshold LET for this integral flux quantity is >1 MeV-cm^2/mg. The spacecraft shielding in these examples is 4 g/cm^2 aluminum, consistent with a lightly shielded aircraft or spacecraft (Singleterry et al., 1999).

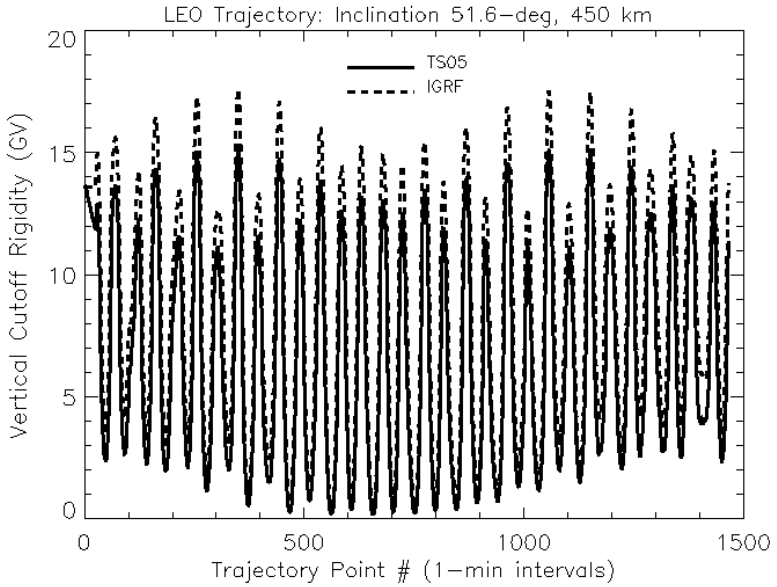

Figure 15: NAIRAS version 3.0 vertical geomagnetic cutoff rigidities for the LEO flight trajectory shown in Figure 13. The datetime of the trajectory at the altitude of 450 km is the 24-hour period from November 2, 2003 16:00 UT to November 3, 2003 16:00 UT. The dashed line shows cutoff rigidities computed using the internal Earth magnetic field only (IGRF). The solid line shows cutoff rigidities computed using both internal and dynamic magnetospheric magnetic field models (IGRF + TS05).

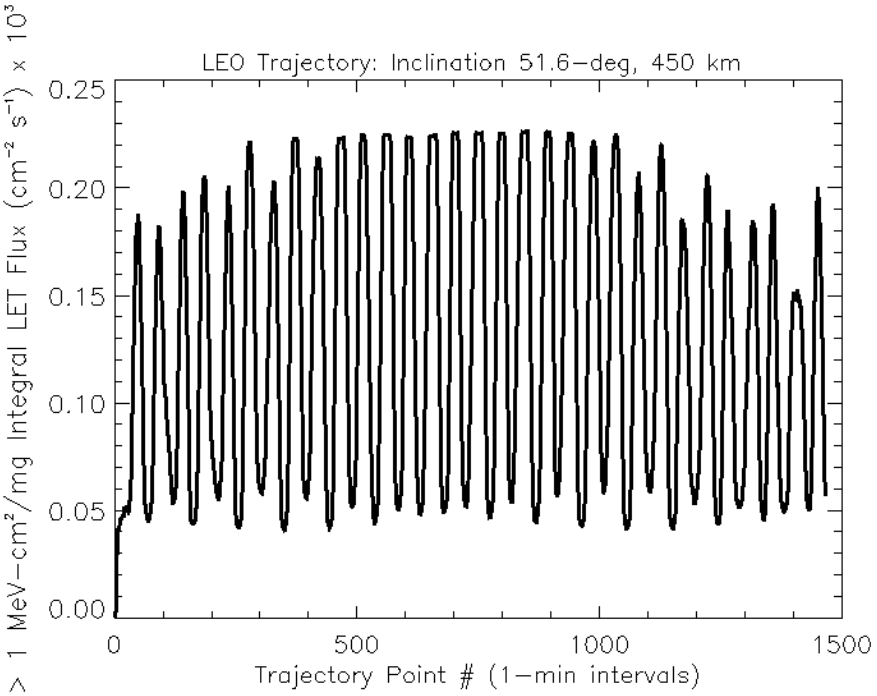

Figure 16: NAIRAS version 3.0 calculation of GCR integral LET flux for the LEO flight trajectory shown in Figure 13. The datetime of the trajectory at the altitude of 450 km is the 24-hour period from November 2, 2003 16:00 UT to November 3, 2003 16:00 UT. The spacecraft shielding is 4 g/cm^2 aluminum.

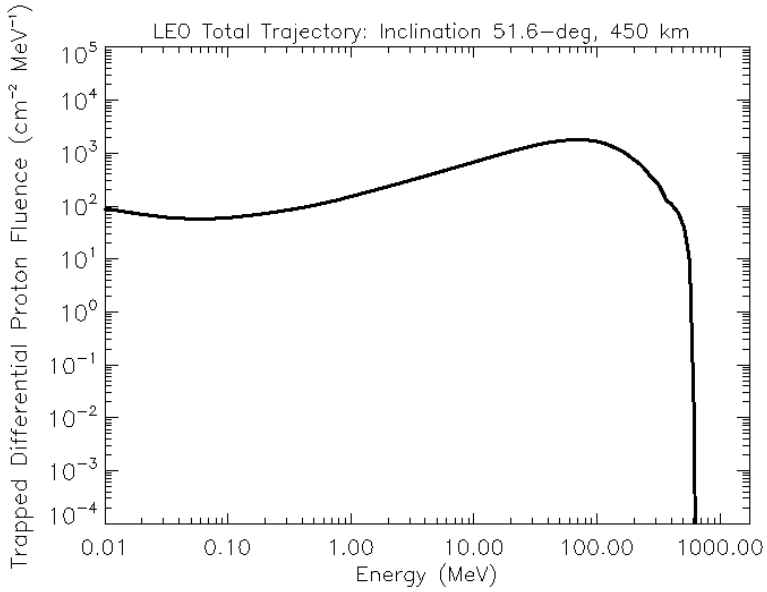

Figure 17: NAIRAS version 3.0 calculation of trapped proton differential fluence for the LEO flight trajectory shown in Figure 13. The datetime of the trajectory at the altitude of 450 km is the 24-hour period from November 2, 2003 16:00 UT to November 3, 2003 16:00 UT. The spacecraft shielding is 4 g/cm^2 aluminum.

The trapped proton differential fluence for the example LEO flight trajectory is shown in Figure 17. By comparing the differential fluence in this figure with the free-space differential flux in Figure 7, one can see the effect of spacecraft shielding in reducing the proton spectrum at low energies. The differential GCR LET fluence for the example LEO flight trajectory is shown in Figure 18. Recall from section 3.1.1 that the ultra-heavy ion composition of the GCR spectrum is responsible for the flux contributions at LET greater than 31.9 MeV-cm^2/mg, which includes energy deposit contributions of GCR nuclei isotopes from copper to uranium.

The next phase in the testing and verification of the model updates in NAIRAS version 3.0 is to characterize the LEO radiation environment for the actual ISS trajectory and for more extended time periods. Thus, the next series of figures are NAIRAS version 3.0 predictions calculated at the ISS orbit during the December 13-16, 2006 SEP events. The ISS trajectory was constructed using python-spg4 and the orbital parameters obtained from the two-line element (TLE) database (space-track.org). The ISS altitude varied between 330-360 km over this four-day period. These SEP events occurred during the annual Fall American Geophysical Union (AGU) meeting and are often referred to the AGU 2006 SEP events. This time period is interesting because ISS experienced a significant attitude control anomaly on December 15, 2006 due to space weather phenomena associated with the AGU 2006 SEP events. The anomaly was attributed to increased atmospheric drag which exceeded the capability of the Control Moment Gyroscope (CMG) system, requiring thrusters to be used instead. There is no evidence of increased SEE rates due to the AGU 2006 SEP radiation enhancement (Koontz et al., 2018). Nevertheless, this event is a good test case to demonstrate the capability of NAIRAS to capture the temporal-spatial variability of the actual space radiation environment, which is needed to quantitatively characterize and assess spacecraft system anomalies.

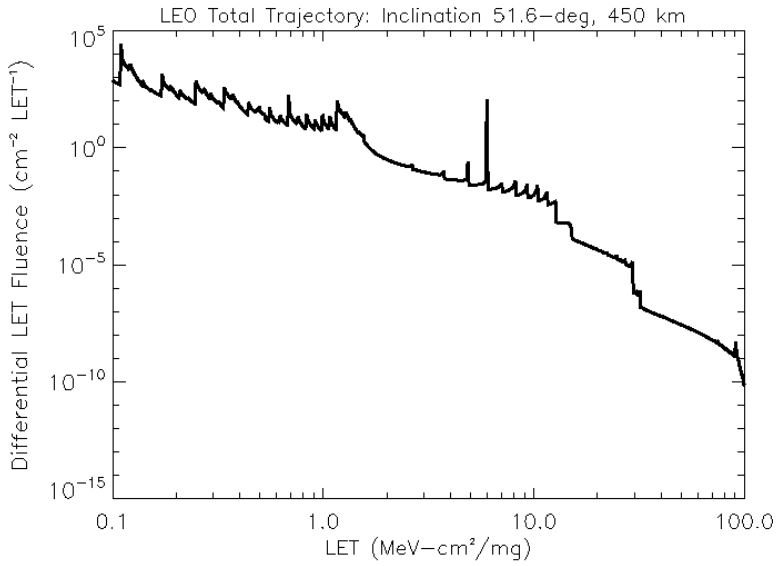

Figure 18: NAIRAS version 3.0 calculation of GCR differential LET fluence for the LEO flight trajectory shown in Figure 13. The datetime of the trajectory at the altitude of 450 km is the 24-hour period from November 2, 2003 16:00 UT to November 3, 2003 16:00 UT. The spacecraft shielding is 4 g/cm^2 aluminum.

The effective dose rates at the ISS orbit during the AGU 2006 SEP events are shown in Figure 19 for a four-day period between December 13-16, 2006. GLE 70 occurred on December 13, 2006 (https://gle.oulu.fi), which corresponds to the largest SEP doses in Figure 19. The largest TRP dose rates occur when the ISS orbit crosses the SAA region. The low-frequency modulations in the GCR dose rates are due to the disturbed interplanetary plasma and IMF (e.g., data from King and Papatashvilli (2013)). The total GCR and TRP effective doses over the four-day period is 1.6 mSv and 127 uSv, respectively, with the combined total effective dose (GCR + TRP) of 1.7 mSv. The total SEP effective dose over the four-day period is 256 uSv, which is roughly 15% of combined GCR + TRP dose.

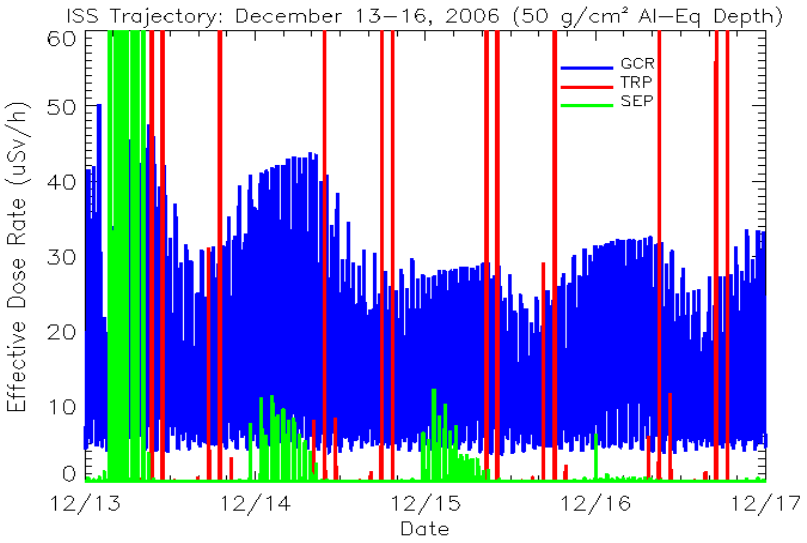

Figure 19: NAIRAS version 3.0 calculation of effective dose rates at the ISS orbit from December 13-16, 2006. The spacecraft shielding is 50 g/cm^2 aluminum.

Integral LET flux is shown in Figure 20 at the ISS orbit for December 13-16, 2006 during the AGU 2006 SEP events. This quantity is an example integral flux quantity that is needed for assessing SEE rates in some space vehicle systems. One of the important features of the NAIRAS model is the ability to capture the actual dynamical variability of the ionizing radiation environment. The integral LET flux has the same low-frequency modulation as the GCR effective dose rates in the previous plot. This appears to be the consequence of a combination of the arrival of an interplanetary shock late on December 14, 2006 and the large scale variability in the IMF components which were also associated with a Forbush decrease (e.g., data from King and Papatashvilli, (2023)).

The SEP differential proton fluence and the SEP integral proton flux, respectively, are shown in the next two figures at the ISS orbit during the AGU 2006 SEP events. These quantities are also useful input quantities to radiation effects models for predicting SEE rates during SEP events. A small amount of shielding significantly reduces the low- energy end of the SEP spectrum, as shown in Figure 21. The results in Figure 22 show that the high-energy tail of the SEP spectrum (> 500 MeV) was elevated during the first SEP event in the series of events that occurred over this four-day storm period, corresponding to GLE 70, and subsequently decayed quite rapidly.

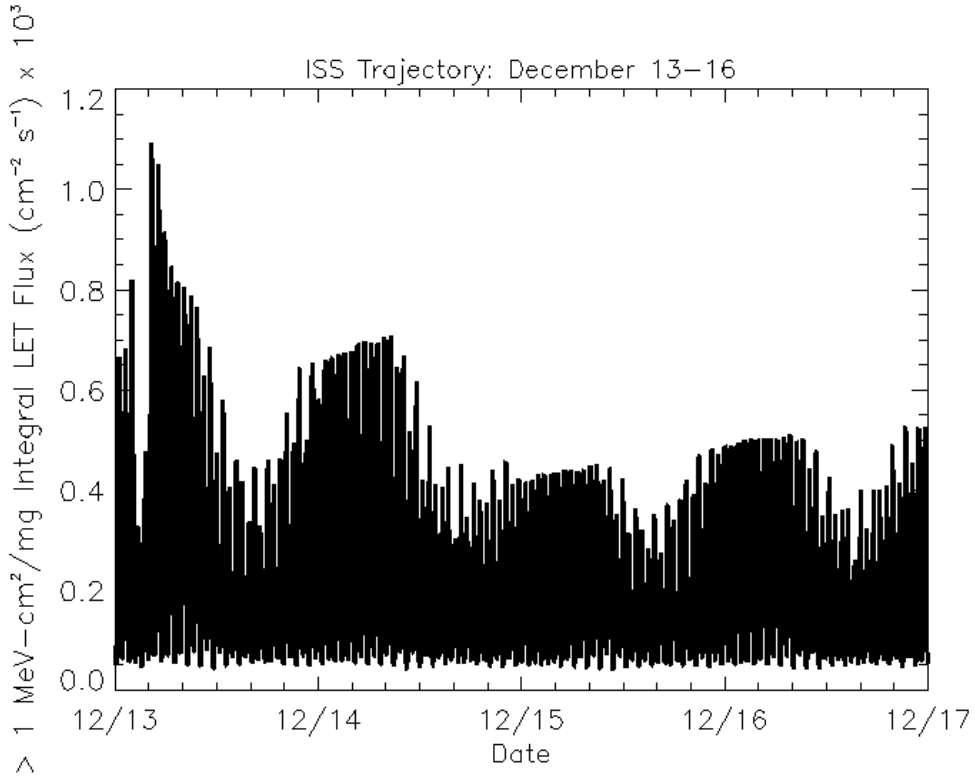

Figure 20: NAIRAS version 3.0 calculation of integral LET flux at the ISS orbit from December 13-16, 2006. The spacecraft shielding is 4 g/cm^2 aluminum.

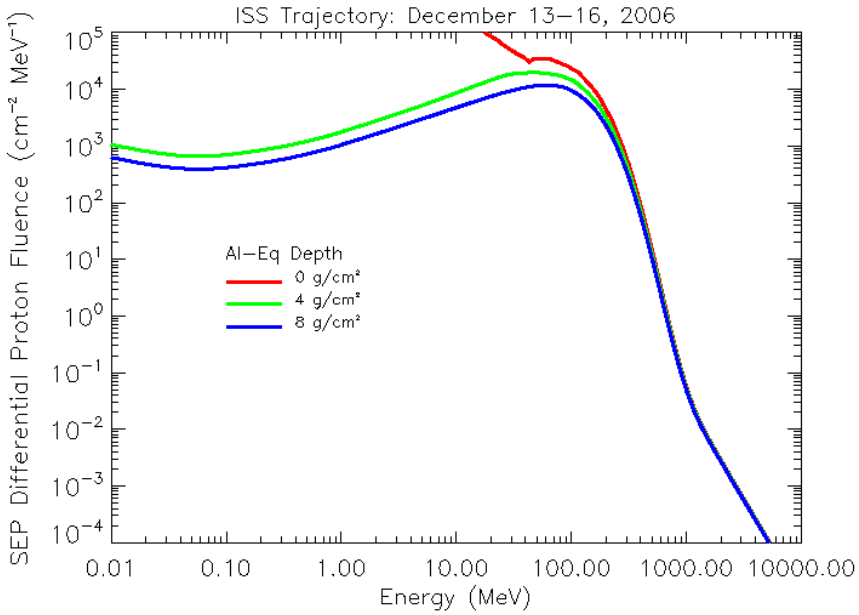

Figure 21: NAIRAS version 3.0 calculation of SEP differential proton fluence at the ISS orbit from December 13-16, 2006.

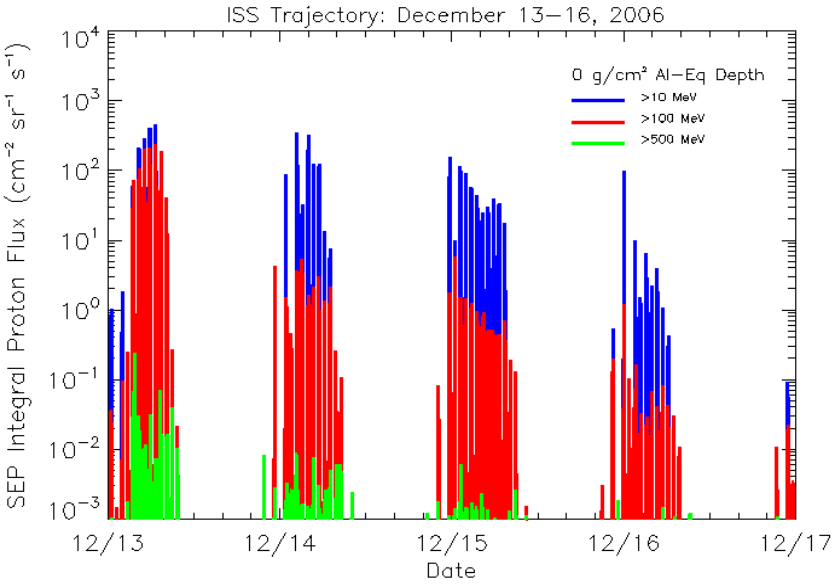

Figure 22: NAIRAS version 3.0 calculation of SEP integral proton flux at the ISS orbit from December 13-16, 2006. The integral flux is shown at several threshold energies and at zero shielding depth.

The Automated Radiation Measurements for Aerospace Safety (ARMAS) dosimeter flight unit, originally developed for continuous aircraft radiation monitoring, has recently been deployed on the ISS (cf., Tobiska et al., 2016). The initial comparisons between the ARMAS ISS measurements and NAIRAS version 3.0 predictions are shown in Figure 23. The NAIRAS TRP dose rates agree with ARMAS measurements quite well. This agreement is encouraging since the TRP model is one of the new features in NAIRAS version 3.0. NAIRAS GCR dose rates also generally agree with ARMAS measurements. In the middle of the time series in Figure 23, NAIRAS underpredicts the ARMAS measurements. Future work will involve additional NAIRAS/ARMAS ISS dose rate comparisons and a detailed investigation of the sources of model-measurement differences.

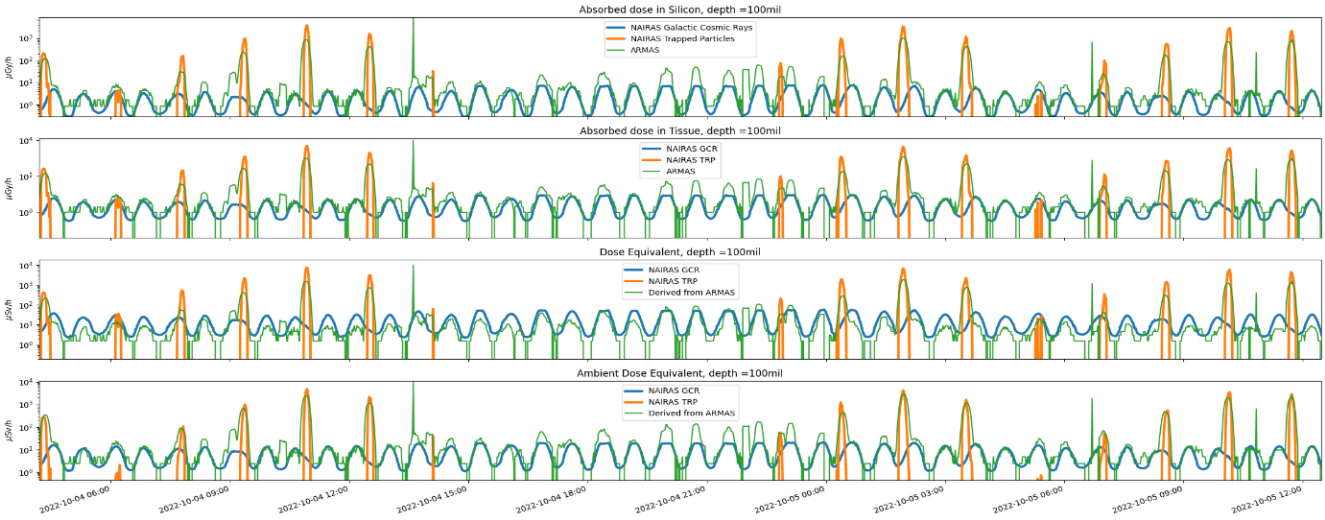

Figure 23: NAIRAS version 3.0 dose calculations and comparisons to ARMAS measurements at ISS from October 4-5, 2022. ARMAS dosimeter shielding is 100 mils of aluminum.

4.2 Medium-Earth Orbit

The NASA Orion Exploration Flight Test 1 (EFT-1) was the first unmanned flight of the Orion Multipurpose Crew Vehicle (MPCV) (Gaza et al., 2017). EFT-1 was launched on December 5, 2014 into a high eccentricity orbit through the radiation belts with a high apogee of ~ 6000 km, orbital inclination of 28.6º, and a total mission duration of 4.5 hours. One of the radiation detector systems flown on EFT-1 was a pair of identical active semiconductor detectors, based on imaging radiation Timepix technology, which was integrated into the Battery-operated Independent Radiation Detector (BIRD) system. The BIRD data analysis algorithm converts measured dose in silicon to dose in water. In Figure 24 is the two BIRD detector measurements (called left and right) of dose rate in water during the EFT-1 flight along with corresponding NAIRAS version 3.0 dosimetric results. NAIRAS dose rate in tissue is the quantity most directly comparable to the BIRD dose rates in water. NAIRAS underestimates the BIRD measurements, but in general the agreement is good.

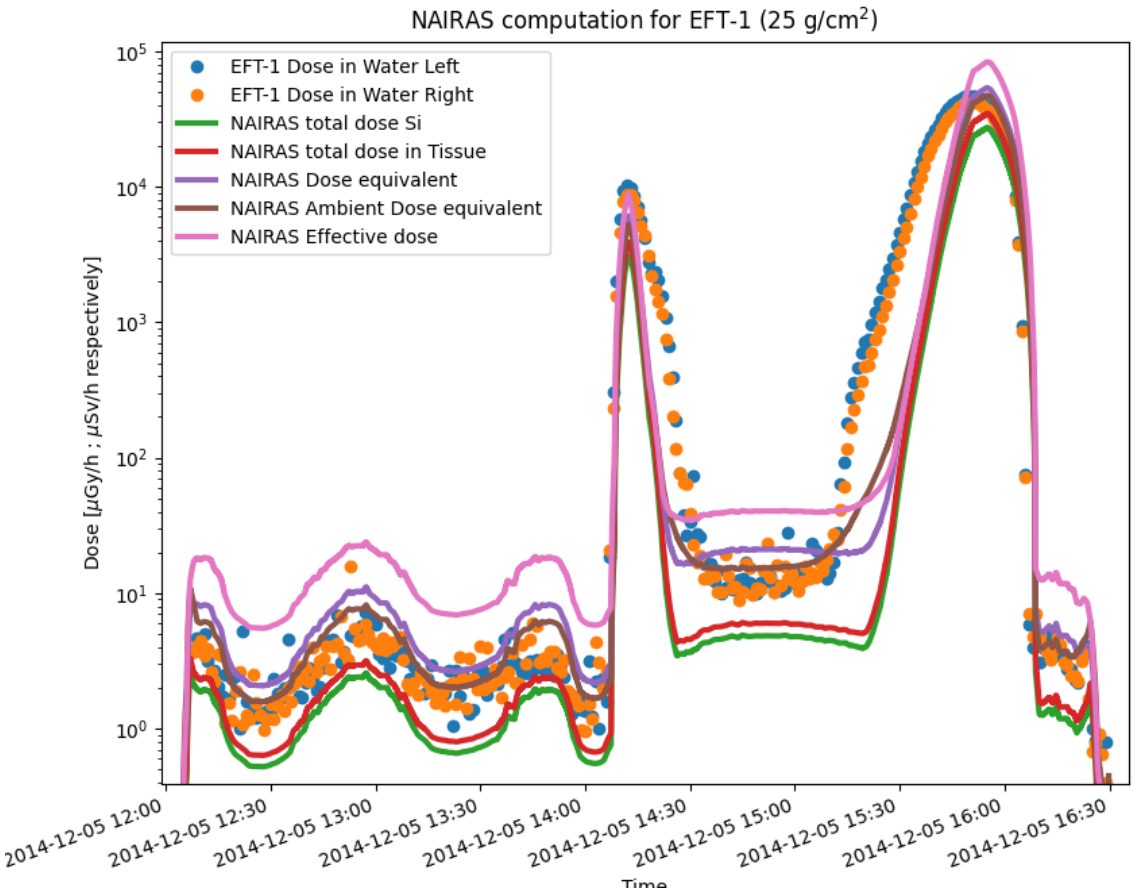

Figure 24: NAIRAS version 3.0 dose calculations and comparisons to BIRD (left and right detectors) measurements at EFT-1 trajectory points on December 5, 2014. The median shielding thickness of the BIRD system is 25 g/cm^2 aluminum-equivalent.

4.3 Cislunar Orbit

The Artemis 1 mission launched on November 16, 2022 was the first spaceflight of NASA's Artemis program. Artemis 1 was a 25-day, uncrewed Moon-orbiting mission, which returned to Earth on December 11, 2022. Using the TLE database, NAIRAS version 3.0 predicted the space radiation environment for the Artemis 1 mission in near real-time. The Orion MPCV was equipped with the Hybrid Electronic Radiation Assessor (HERA), which is a distributed dosimeter system based on the coupling of a solid-state silicon detector with a Timepix chip (Kroupa et al., 2015). Future work will involve detailed comparisons between NAIRAS version 3.0 results and HERA measurements along the Artemis 1 flight trajectory. The results shown in Figure 25 are graphical products of the near real-time NAIRAS version 3.0 dosimetric predictions during the Artemis 1 flight computed at the median shielding thicknesses of the HERA dosimeters on the Orion MPCV (Mertens et al., 2018), focusing on the launch to free-space phase of the flight trajectory.

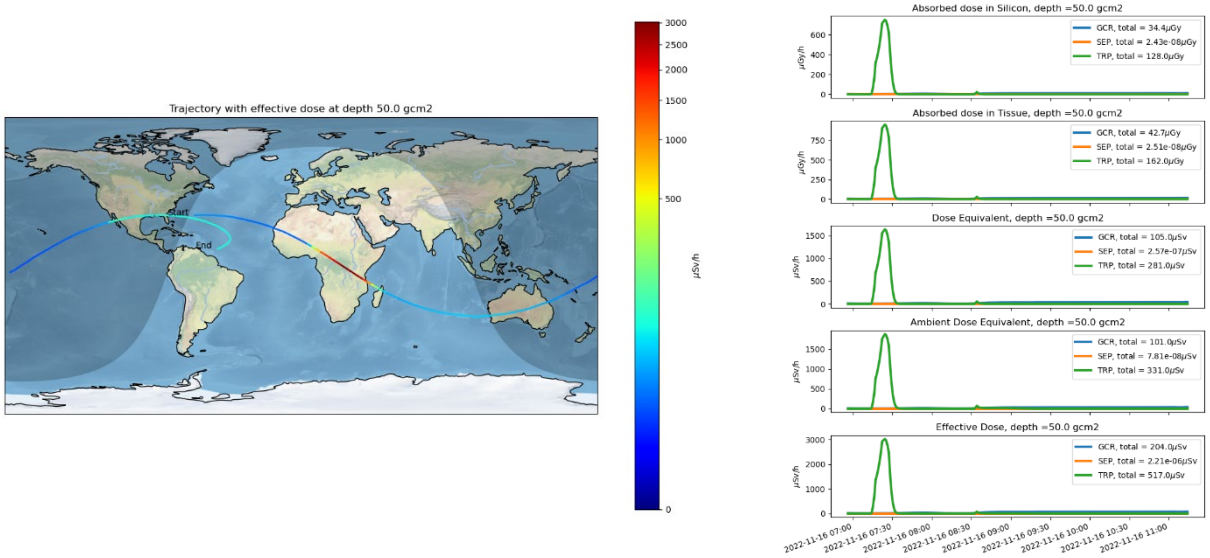

Figure 25: NAIRAS version 3.0 dosimetric predictions during the NASA Artemis 1 flight mission on November 16, 2022. The results focus on the launch to free-space phase of the flight trajectory. The dosimetric quantities are shown for 50 g/cm^2 aluminum shielding.

5.0 Conclusions

The NAIRAS version 3.0 RoR capability allows end-users to run the model for customized scenarios and to perform scientific and engineering analysis of the atmospheric and space radiation environments. The global dosimetric run option provides context and situational awareness of the atmospheric ionizing radiation environment. The flight trajectory run option allows detailed human radiation flight exposure characterization, detailed comparisons to onboard dosimeters, and the assessment of SEE in aircraft and spaceflight electronic systems.

NAIRAS version 3.0 developments also included important model extensions and improvements. The domain of the model was extended from the atmosphere to free-space. The multi-directional transport procedure implemented for atmospheric ionizing radiation modeling significantly improved the accuracy of the dosimetric quantities at altitudes above 15 km. Analysis of the dosimetric measurements taken during the RaD-X campaign and measurements from the 1000+ ARMAS aircraft flights over the last decade show that the NAIRAS version 3.0 predictions agree with measurement to within 30% from 0-40 km. Publications of these results are in preparation. The robustness and fidelity of the SEP proton spectral fitting algorithm has been significantly improved by fitting to the GOES integral proton flux measurements. The geomagnetic vertical cutoff rigidity model was extended to include the option of two magnetospheric magnetic field models. This update facilitates intercomparisons between different cutoff and radiation models and provides a modeling framework for developing a cutoff rigidity forecast model. The improvements in the computational efficiency of the SEP proton spectral fitting algorithm and the vertical cutoff model enables NAIRAS version 3.0 predictions to be performed at 5-minute time-intervals with reasonable and practical turnaround times.

The next phase of NAIRAS version 3.0 updates will focus on developing a SEP heavy-ion model and additional validation studies of the NAIRAS model in the geospace and free-space

radiation environments. The SEP heavy-ion model will enable NAIRAS to predict SEP LET spectra out to 100 MeV-cm^2/gm, which is important to characterize SEE in spacecraft electronic systems during SEP events. A few preliminary validation results have been shown in this paper for LEO and MEO. Validation studies and analysis of NAIRAS version 3.0 in the space radiation environment will be extended in future work, as well as comparisons with the HERA dose measurements onboard the Artemis 1 flight.

Appendix A: SEP Spectral Fitting Algorithm

The objective of the SEP proton spectral fitting algorithm is to determine the free parameters of the analytical forms in equations (5)-(8) that optimally estimate the GOES proton flux measurements to within measurement uncertainty. The problem statement can be formally expressed as

$$\mathbf{y} = \mathbf{F}(\mathbf{x}) + \boldsymbol{\varepsilon}, \tag{28}$$

where $\mathbf{y}$ is the vector of GOES proton flux measurements, $\mathbf{F}(\mathbf{x})$ is the model of the measurements, or the so-called forward model, which depends on the parameter vector $\mathbf{x}$, and $\boldsymbol{\varepsilon}$ is the vector of measurement errors. Assuming Gaussian noise statistics for $\boldsymbol{\varepsilon}$, a maximum likelihood solution for the free parameters $\mathbf{x}$ can be found by solving a Bayesian statistical inverse problem (e.g., Mertens et al., 2018). This is equivalent to finding a solution $\mathbf{x_s}$ that minimizes the cost function $\Phi(\mathbf{x})$, such that

$$\nabla\Phi(\mathbf{x_s}) = 0, \tag{29}$$

with the cost function given by

$$\Phi(\mathbf{x}) = \left(\mathbf{y} - \mathbf{F}(\mathbf{x})\right)^T \tilde{\mathbf{S}}_\varepsilon^{-1} \left(\mathbf{y} - \mathbf{F}(\mathbf{x})\right), \tag{30}$$

and the measurement error covariance matrix denoted $\tilde{\mathbf{S}}_\varepsilon$. The forward model can be expanded in a Taylor series to first order about an initial guess for the model parameters $\mathbf{x_0}$, such that

$$\mathbf{F}(\mathbf{x}) = \mathbf{F}(\mathbf{x}_0) + \frac{\partial \mathbf{F}}{\partial \mathbf{x}}\left(\mathbf{x} - \mathbf{x}_0\right) + \cdots \tag{31}$$

$$\mathbf{F}(\mathbf{x}) \approx \mathbf{F}(\mathbf{x}_0) + \tilde{\mathbf{K}}(\mathbf{x} - \mathbf{x}_0), \tag{32}$$

where $\tilde{\mathbf{K}}$ is the Jacobian matrix, or sometimes referred to as the measurement weighting function (Mertens et al., 2018). For a linear problem, the solution for the free parameters $\mathbf{x}_s$ can be obtained in one solution step by solving equation (29) and equation (30) with the forward model given by equation (32). However, for forward models with a nonlinear dependence on the model parameters, a Newtonian iteration of the linear solution is typically employed until convergence is reached. For moderately nonlinear problems, a Marquardt-Levenberg approach improves the convergence of the Newtonian iteration method by introducing an optimally-determined parameter λ into the solution equation (Press et al., 1992). Thus, the Marquardt-Levenberg solution of equation (29) and equation (30) can be expressed in the following form:

$$\mathbf{x}_i = \mathbf{x}_{i-1} + \left(\tilde{\mathbf{K}}_{i-1}^T \tilde{\mathbf{S}}_\varepsilon^{-1} \tilde{\mathbf{K}}_{i-1} + \lambda_{i-1} \tilde{\mathbf{I}}\right)^{-1} \left[\tilde{\mathbf{K}}_{i-1}^T \tilde{\mathbf{S}}_\varepsilon^{-1} \tilde{\mathbf{K}}_{i-1} \left(\mathbf{y} - \mathbf{F}(\mathbf{x}_{i-1})\right)\right], \tag{33}$$

where the subscript denotes the iteration step. The Marquardt-Levenberg algorithm determines the λ parameter at each iteration step to give a steepest descent increment when far from the solution and an inverse Hessian increment when near the solution (Press et al., 1992). The Marquardt-Levenberg algorithm used in the NAIRAS version 3.0 SEP spectral fitting code is an adaptation of the routines reported by Brandt (1999).

The application of the general expression in equation (33) to SEP proton spectral fitting to GOES differential proton flux measurements is described as follows. The measurement vector $\mathbf{y}$ is the GOES differential proton flux measurements. The number of GOES differential proton channels used in the SEP proton spectral fit is typically around seven with average channel energies varying between 25 MeV and 600 MeV, depending on the specific GOES series and its particle flux detector system. The forward model $\mathbf{F}(\mathbf{x})$ is the analytical SEP proton spectral forms in equations (5)-(8) evaluated at the geometric average energy of the GOES differential proton flux channels. The measurement error covariance matrix $\tilde{\mathbf{S}}_{\varepsilon}$ is prescribed by uncorrelated Poisson statistics. Computational efficiency and numerical accuracy and stability are maximized when the Jacobian matrix is computed analytically. Thus, the Jacobian matrices for the four analytical representations of the SEP proton spectral flux are given below.

For the single power-law representation of the SEP proton spectral flux in equation (5), let the parameter vector be defined as $\mathbf{x} = \left(C, \gamma\right)^T$. The Jacobian matrix elements for the fit to GOES differential proton flux are:

$$\begin{aligned} \tilde{\mathbf{K}}_{1,j} &= E_j^{-\gamma} \\ \tilde{\mathbf{K}}_{2,j} &= -CE_j^{-\gamma} \ln E_j. \end{aligned} \tag{34}$$

For the Ellison-Ramaty representation of the SEP proton spectral flux in equation (6), let the parameter vector be defined as $\mathbf{x} = \left(C, \gamma, E_0\right)^T$. The Jacobian matrix elements for the fit to GOES differential proton flux are:

$$\begin{aligned} \tilde{\mathbf{K}}_{1,j} &= E_j^{-\gamma} \exp(-E_j / E_0) \\ \tilde{\mathbf{K}}_{2,j} &= -CE_j^{-\gamma} \exp(-E_j / E_0) \ln E_j \\ \tilde{\mathbf{K}}_{3,j} &= C\left(E_j / E_0\right)^2 E_j^{-\gamma-1} \exp(E_j / E_0). \end{aligned} \tag{35}$$

For the Ellison-Ramaty double power-law representation of the SEP proton spectral flux in equation (7), let the parameter vector be defined as $\mathbf{x} = \left(C, \gamma_a, E_0, \gamma_b\right)^T$. The Jacobian matrix elements for the fit to GOES differential proton flux are:

$$
\begin{aligned}
\tilde{\mathbf{K}}_{1,j} &= E_j^{-\gamma_a} \exp(-E_j / E_0) \text{ for } E_j \le (\gamma_b - \gamma_a) E_0 \\
&= E_j^{-\gamma_b} \left\{ \left[(\gamma_b - \gamma_a) E_0 \right]^{(\gamma_b - \gamma_a)} \exp(\gamma_a - \gamma_b) \right\} \text{ for } E_j > (\gamma_b - \gamma_a) E_0 \\
\tilde{\mathbf{K}}_{2,j} &= -C E_j^{-\gamma_a} \exp(-E_j / E_0) \ln E_j \text{ for } E_j \le (\gamma_b - \gamma_a) E_0 \\
&= -C E_j^{-\gamma_b} \left\{ \left[(\gamma_b - \gamma_a) E_0 \right]^{(\gamma_b - \gamma_a)} \exp(\gamma_a - \gamma_b) \right\} \ln \left[(\gamma_b - \gamma_a) E_0 \right] \text{ for } E_j > (\gamma_b - \gamma_a) E_0 \\
\tilde{\mathbf{K}}_{3,j} &= C (E_j / E_0)^2 E_j^{-\gamma_a - 1} \exp(E_j / E_0) \text{ for } E_j \le (\gamma_b - \gamma_a) E_0 \\
&= C E_j^{-\gamma_b} \left\{ \left[(\gamma_b - \gamma_a) E_0 \right]^{(\gamma_b - \gamma_a)} \exp(\gamma_a - \gamma_b) \right\} \left\{ \frac{(\gamma_b - \gamma_a)}{E_0} \right\} \text{ for } E_j > (\gamma_b - \gamma_a) E_0 \\
\tilde{\mathbf{K}}_{4,j} &= 0 \text{ for } E_j \le (\gamma_b - \gamma_a) E_0 \\
&= C E_j^{-\gamma_b} \left\{ \left[(\gamma_b - \gamma_a) E_0 \right]^{(\gamma_b - \gamma_a)} \exp(\gamma_a - \gamma_b) \right\} \ln \left[\frac{(\gamma_b - \gamma_a) E_0}{E_j} \right] \text{ for } E_j > (\gamma_b - \gamma_a) E_0 .
\end{aligned}
\tag{36}
$$

For the Weibull representation of the SEP proton spectral flux in equation (8), let the parameter vector be defined as $\mathbf{x} = (C, k, \gamma)^T$. The Jacobian matrix elements for the fit to GOES differential proton flux are:

$$
\begin{aligned}
\tilde{\mathbf{K}}_{1,j} &= k\gamma E_j^{\gamma - 1} \exp\left(-k E_j^{\gamma}\right) \\
\tilde{\mathbf{K}}_{2,j} &= C k \gamma E_j^{\gamma - 1} \exp\left(-k E_j^{\gamma}\right) \left[\frac{1}{k} - E_j^{\gamma} \right] \\
\tilde{\mathbf{K}}_{3,j} &= C k \gamma E_j^{\gamma - 1} \exp\left(-k E_j^{\gamma}\right) \left[\frac{1}{\gamma} + \ln E_j - k E_j^{\gamma} \ln E_j \right].
\end{aligned}
\tag{37}
$$

The convergence of the Marquardt-Levenberg algorithm for the solution of the parameter vector in equation (33) is based on the difference in the chi-square solution residual χ^2 between successive iteration steps (Brandt, 1999). The convergence criterion on the successive chi-square residuals is explicitly

$$
\left| \chi_i^2 - \chi_{i-1}^2 \right| < \varepsilon \left| \chi_{i-1}^2 \right| + \delta \tag{38}
$$

where $\varepsilon = 10^{-8}$ and $\delta = 10^{-15}$.

The NAIRAS version 3.0 SEP spectral fitting algorithm fits all four analytical representations of the SEP proton spectrum in equations (5)-(8) using the methodology described in this section. The analytical form that has the minimum chi-square residual out of the four spectral representations is selected as the potential optimal solution spectrum. One further test criterion is applied. If the reduced chi-square residual is less than 1.0, then the selected potential spectrum is the final optimal solution for the SEP proton spectrum used in the subsequent NAIRAS SEP transport and response function calculations. If the solution spectrum does not pass the final goodness test, the SEP proton spectrum is formed by log-log interpolation and extrapolation of the GOES differential proton flux measurements. A hard limit on the

extrapolated flux at high-energy is also set. Based on experience and numerous SEP event test cases, if the extrapolated flux at 10 GeV is greater than 10^{-7} $(cm^2\text{-MeV-sr-s})^{-1}$, then the SEP spectral flux is set to a numerically small value at all energies greater than or equal to the highest energy GOES differential proton channel.

The SEP proton spectral fitting approach to GOES integral proton flux measurements is described next. The measurement vector $\mathbf{y}$ is the vector of GOES integral proton flux measurements. The number of GOES integral proton channels used in the SEP proton spectral fit is six or seven, depending on the specific GOES series and its particle flux detector system, with threshold energies between >10 MeV and >700 MeV. The measurement error covariance matrix $\tilde{\mathbf{S}}_{\varepsilon}$ is prescribed by uncorrelated Poisson statistics. The forward model $\mathbf{F}(\mathbf{x})$ is the analytical SEP proton spectral forms in equations (5)-(8) integrated from the threshold energies of the GOES integral proton flux channels to infinity. Thus, the analytical representations of SEP integral proton flux for single power-law, Ellison-Ramaty, Ellison-Ramaty double power-law, and Weibull spectral forms are given, respectively, by

$$J_{SP}(E) = \left(\frac{C}{\gamma - 1}\right) E^{1-\gamma} \tag{39}$$

$$J_{ER}(E) = C E_0^{1-\gamma} \Gamma(1-\gamma, E/E_0) \tag{40}$$

$$\begin{aligned} J_{DP}(E) &= C E_0^{1-\gamma_a} \left[\Gamma(1-\gamma_a, E/E_0) - \Gamma(1-\gamma_a, \gamma_b - \gamma_a)\right] \\ &\quad + \left(\frac{C}{\gamma_b - 1}\right) \left[\left(\gamma_b - \gamma_a\right) E_0\right]^{1-\gamma_b} \left\{\left[\left(\gamma_b - \gamma_a\right) E_0\right]^{(\gamma_b - \gamma_a)} \exp\left(\gamma_a - \gamma_b\right)\right\} \text{ for } E \le \left(\gamma_b - \gamma_a\right) E_0 \\ &= \left(\frac{C}{\gamma_b - 1}\right) E^{1-\gamma_b} \left\{\left[\left(\gamma_b - \gamma_a\right) E_0\right]^{(\gamma_b - \gamma_a)} \exp\left(\gamma_a - \gamma_b\right)\right\} \text{ for } E > \left(\gamma_b - \gamma_a\right) E_0 \end{aligned} \tag{41}$$

$$J_{WB}(E) = C \exp\left(-kE^{\gamma}\right). \tag{42}$$

In equations (40) and (41), $\Gamma(a,x)$ is the complement of the incomplete gamma function, which is defined as

$$\Gamma(a,x) = \int_x^{\infty} t^{a-1} e^{-t} dt. \tag{43}$$

Equation (43) can be expressed in terms of the gamma function and the incomplete gamma function, such that

$$\Gamma(a,x) = \Gamma(a) - \gamma(a,x), \tag{44}$$

where the gamma function and incomplete gamma function are defined by

$$\Gamma(a) = \int_0^{\infty} t^{a-1} e^{-t} dt \quad [\mathrm{Re}(a) > 0] \tag{45}$$

and

$$\gamma(a,x) = \int_0^x t^{a-1} e^{-t} dt \quad [\mathrm{Re}(a) > 0], \tag{46}$$

respectively. The NAIRAS version 3.0 SEP spectral fitting algorithm uses the computationally efficient numerical algorithms for evaluating the complement of the incomplete gamma function developed by Zhang and Jin (1996), which are based on the relationships in equations (43)-(46). Another property of the complement of the incomplete gamma function important for deriving analytical expressions for the Jacobian matrix is the derivative with respect to its variable argument, which is given by (Zhang & Jin, 1996)

$$\frac{d\Gamma(a,x)}{dx} = -x^{a-1} e^{-x}. \tag{47}$$

Analytical computation of the Jacobian matrix in spectral fitting to GOES integral proton flux measurements is essential to the computational efficiently necessary to fit the SEP proton spectrum at 5-minute time intervals throughout the time evolution of a SEP event. Thus, the Jacobian matrices for the four analytical representations of the SEP integral proton flux are described below.

For the single power-law representation of the SEP integral proton flux in equation (39), let the parameter vector be defined as $\mathbf{x} = \left(C, \gamma\right)^T$. The Jacobian matrix elements for the fit to GOES integral proton flux are:

$$\begin{aligned} \tilde{\mathbf{K}}_{1,j} &= J_{SP}(E_j) / C \\ \tilde{\mathbf{K}}_{2,j} &= -J_{SP}(E_j) \left[\frac{1}{\gamma - 1} + \ln E_j \right] \end{aligned} \tag{48}$$

For the Ellison-Ramaty representation of the SEP integral proton flux in equation (40), let the parameter vector be defined as $\mathbf{x} = \left(C, \gamma, E_0\right)^T$. The Jacobian matrix elements for the fit to GOES integral proton flux are:

$$\begin{aligned} \tilde{\mathbf{K}}_{1,j} &= J_{ER}(E_j) / C \\ \tilde{\mathbf{K}}_{2,j} &= -J_{ER}(E_j) \ln E_0 + \frac{J_{ER}(E_j)}{\Gamma(1-\gamma, E_j / E_0)} \left[\frac{\Gamma(1-\gamma-\Delta\gamma, E_j / E_0) - \Gamma(1-\gamma, E_j / E_0)}{\Delta\gamma} \right] \\ \tilde{\mathbf{K}}_{3,j} &= \left(\frac{J_{ER}(E_j)}{E_0} \right) \left[(1-\gamma) + \frac{\left(E_j / E_0\right)^{(1-\gamma)}}{\Gamma(1-\gamma, E_j / E_0)} \exp\left(-E_j / E_0\right) \right]. \end{aligned} \tag{49}$$

The derivative of the complement of the incomplete gamma function with respect to the parameter argument for the $\tilde{\mathbf{K}}_{2,j}$ elements is computed numerically where $\Delta\gamma = 0.1\gamma$ in the code.

For the Weibull representation of the SEP integral proton flux in equation (42), let the parameter vector be defined as $\mathbf{x} = \left(C, k, \gamma\right)^T$. The Jacobian matrix elements for the fit to GOES integral proton flux are:

$$\begin{aligned} \tilde{\mathbf{K}}_{1,j} &= J_{WB}(E_j)/C \\ \tilde{\mathbf{K}}_{2,j} &= -J_{WB}(E_j)E_j^{\gamma} \\ \tilde{\mathbf{K}}_{3,j} &= -J_{WB}(E_j)kE_j^{\gamma}\ln E_j . \end{aligned} \tag{50}$$

The analytical expression for the Jacobian matrix for the forward model of integral flux of the Ellison-Ramaty double power-law spectral form is quite complex. In fact, the number of evaluations of the complement of the incomplete gamma function and its numerical derivative with respect to the parameter argument offset the computational advantage of an analytical Jacobian matrix evaluation. Thus, for this case the Jacobian matrix is evaluated numerically, which requires a numerical evaluation of the derivative of the forward model with respect to the fit parameters, according to the definition of the Jacobian matrix in equations (31)-(32). The derivative is computed very accurately by employing a Richardson extrapolation technique, which successively reduces term-by-term the truncation error (Hildebrand, 1974). Note, the evaluation of the forward model is still computed using the analytical representation in equation (41). The convergence criterion of the numerical calculation of the Jacobian matrix elements is

$$\left|\Delta\tilde{\mathbf{K}}_{i,j}\right| \le \varepsilon \text{ or } \left|\Delta\tilde{\mathbf{K}}_{i,j}\right| \le \delta\left|\tilde{\mathbf{K}}_{i,j}\right| \tag{51}$$

where $\varepsilon = 10^{-10}$ and $\delta = 5\text{x}10^{-8}$. In the equation (51), $\Delta\tilde{\mathbf{K}}_{i,j}$ is the difference in the numerical computation of the Jacobian matrix element between successive iterations in the Richardson extrapolation method (cf., Brandt, 1999).

Analogous to SEP spectral fitting to the GOES differential proton flux channels, the NAIRAS version 3.0 algorithm fits all four analytical representations of the SEP proton spectrum in equations (5)-(8) to the GOES integral proton flux channels using the approach described in the previous paragraphs. The analytical form that has the minimum chi-square residual out of the four spectral representations is selected as the potential optimal solution for the SEP proton spectrum. An additional goodness criterion is applied. If the reduced chi-square residual is less than 1.0, then the selected potential spectrum is the final optimal solution for the SEP proton spectrum used in the subsequent NAIRAS SEP transport and response function calculations. If the solution spectrum does not pass the final goodness test, the SEP proton spectrum is approximated using an integral flux derivative approach.

The integral flux derivative approach is described as follows. The GOES integral proton flux measurements are spline interpolated to a high-resolution energy grid (20 points per decade in energy). Numerical first-order derivatives of the integral flux data are computed on the high-resolution energy grid to convert integral flux to differential (spectral) flux. A box car smoothing is applied to remove numerical ringing from the derivative calculation. The calculated spectrum is then interpolated to the (courser) internal NAIRAS SEP transport energy grid. As a standalone method, this approach is accurate and robust for large SEP events, as verified by comparisons of the derived SEP proton spectrum from this approach with the GOES differential

proton flux measurements. The disadvantage of this approach is that it does not permit estimates of solution error characteristics like the Bayesian statistical inverse method does. On the other hand, from numerous SEP event test cases spanning the range of quiet conditions (no SEP) to weak and strong SEP events, one of the four analytical representations of the SEP proton spectrum in equations (5)-(8) has never failed to meet the convergence and goodness criteria described in this Appendix when fitting to the GOES integral proton flux measurements.

References

Adriani, O., Barbarino, G. C., Bazilevskaya, G. A., Bellotti, R. Boizio, M., Bogomolov, E. A., et al. (2013). Time dependence of the proton flux measured by PAMELA during the 2006 July – 2006 December Solar Minimum. *The Astrophysical Journal*, 765(91), doi:10.1088/0004-637X/765/2/91

Adriani, O., Barbarino, G. C., Bazilevskaya, G. A., Bellotti, R. Boizio, M., Bogomolov, E. A., et al. (2016). Measurements of cosmic-ray hydrogen and helium isotopes with the PAMELA experiment. *The Astrophysical Journal*, 818(68), doi:10.3847/0004-637X/818/1/68

Badavi, F. F., Nealy, J. E., & Wilson, J. W. (2011). The low earth orbit validation of a dynamic and anisotropic trapped radiation model through ISS measurements. *Advances in Space Research*, 48, 1441-1458.

Binns, W. R., Fickle, R. K., Garrard, T. L., Israel, M. H., Klarmann, J., Stone, E. C., & Waddington, C. J. (1982). The abundance of the actinides in the cosmic radiation as measured on HEAO 3. *The Astrophysical Journal*, 261, L117-L120.

Brandt, S. (1999). *Data analysis, statistical and computational methods for scientists and engineers*. New York, New York: Springer-Verlag.

Cucinotta, F. A., Kim, M.-H. Y., Willingham, V., & George, K. A. (2008). Physical and biological organ dosimetry analysis for International Space Station astronauts. *Radiation Research*, 170, 127-138, doi:10.1667/RR1330.1

Ellison, D. C., & Ramaty, R. (1985). Shock acceleration of electrons and ions in solar flares. *The Astrophysical Journal*, 298, 400-408.

Fowler, P. H., Walker, R. N. F., Masheder, M. R. W., Moses, R. T., Worley, A., & Gay, A. M. (1987). Ariel 6 measurements of the fluxes of ultraheavy cosmic rays. *The Astrophysical Journal*, 314, 739-746.

Gaza, R., Kroupa, M., Rios, R., Stoffle, N., Benton, E. R., & Semones, E. J. (2017). Comparison of novel active semiconductor pixel detector with passive radiation detectors during the NASA Orion Exploration Flight Test 1 (EFT-1). *Radiation Measurements*, 106, 290-297, http://dx.doi.org/10.1016/j.radmeas.2017.03.041

Hands, A. D. P., Ryden, K. A., & Mertens, C. J. (2016). The disappearance of the Pfotzer-Regener maximum in dose equivalent measurements in the stratosphere. *Space Weather*, 14, 776-785, doi:10.1002/2016SW001402

Heynderickx, D., Lemaire, J., & Daly, E. J. (1996). Historical review of the different procedures used to compute the L-parameter. *Radiation Measurements*, 26(3), 325-331.

Hu, S., Kim, M.-H. Y., McClellan, G. E., & Cucinotta, F. A. (2009). Modeling the acute health effects of astronauts from exposure to large solar particle events. *Health Physics*, 96(4), 1-12.

Hildebrand, F. B. (1974). *Introduction to numerical analysis*. New York: Dover Publications, Inc.

King, J. H., & Papatashvilli, N. (2023). OMNI Combined, Definitive, 5-minute IMF and Plasma, and Energetic Proton Fluxes., Time-Shifted to the Nose of the Earth's Bow Shock, Plus Magnetic Indices. OMNI_HRO_5MIN [Dataset]. AdnetSystems, NASA Goddard Space Flight Center and CDAWeb (select OMNI and select OMNI_HRO_5MIN). SPDF - Coordinated Data Analysis Web (CDAWeb) (nasa.gov)

Koontz, S., Suggs, R., Alred, J., Worthy, E., Boeder, P., Steagall, C., et al. (2018). *The International Space Station space radiation environment: Avionics systems performance in low-Earth orbit single event effects environments (SEE)*. Paper presented at the 48th International Conference on Environmental Systems (ICES-2018-69), Albuquerque, New Mexico.

Kress, B. T., Hudson, M. K., Perry, K. L., & Slocum, P. L. (2004). Dynamic modeling of geomagnetic cutoff for the 23-24 November 2001 solar energetic particle event. *Geophysical Research Letters*, 31, L04808, doi:10.1029/2003GL018599

Kress, B. T., Mertens, C. J., & Wiltberger, M. (2010). Solar energetic particle cutoff variations during the 28-31 October 2003 geomagnetic storm. *Space Weather*, 8, S05001, doi:10.1029/2009SW000488

Kroupa, M., Bahadori, A., Campbell-Ricketts, T., Empl, A., Hoang, S. M., Idrraga-Munoz, J, et al. (2015). A semiconductor radiation imaging detector for space radiation dosimetry. *Life Sciences in Space Research*, 6, 69-78.

Mertens, C. J., Kress, B. T., Wiltberger, M., Blattnig, S. R., Slaba, T. S., Solomon, S. C., & Engel, M. (2010). Geomagnetic influence on aircraft radiation exposure during a solar energetic particle event in October 2003. *Space Weather,* 8, S03006, doi:10.1029/2009SW000487

Mertens, C.J., Kress, B. T., Wiltberger, M., Tobiska, W. K., Grajewski, B., & Xu, X. (2012). Atmospheric ionizing radiation from galactic and solar cosmic rays. In M. Nenoi (Ed.), *Current topics in ionizing radiation research* (pp. 683-738). Rijeka, Croatia: InTech Publisher.

Mertens, C. J., Meier, M. M., Brown, S., Norman, R. B., & Xu, X. (2013). NAIRAS aircraft radiation model development, dose climatology, and initial validation. *Space Weather*, 11, 603–635, doi:10.1002/swe.20100

Mertens, C. J. (2016a). Overview of the Radiation Dosimetry Experiment (RaD-X) flight mission. *Space Weather*, 14, doi:10.1002/2016SW001399

Mertens, C. J., Gronoff, G. P., Norman, R. B., Hayes, B. M., Lusby, T. C., Straume, T., et al. (2016b). Cosmic radiation measurements from the RaD-X flight campaign. *Space Weather*, 14, 874-898, doi:10.1002/2016SW001407

Mertens, C. J., Slaba, T. C., & Hu, S. (2018). Active dosimetric-based estimate of astronaut acute radiation risk for real-time solar energetic particle events. *Space Weather*, 16, 1291-1316, https://doi.org/10.1029/2018SW001971

Mertens, C. J., & Slaba, T. C. (2019). Characterization of solar energetic particle radiation dose to astronaut crew on deep-space exploration mission. *Space Weather*, 14, https://doi.org/10.1029/2019SW002363

Mewaldt, R. A. (1988). Elemental composition and energy spectra of galactic cosmic rays. In *Interplanetary Particle Environment* (JPL Publication 88, pp. 121-132). Pasadena, CA: Jet Propulsion Laboratory, California Institute of Technology.

Mewaldt, R. A., Cohen, C. M. S., Labrador, A. W., Leske, R. A., Mason, G. M., Desai, M. I., et al. (2005). Proton, helium, and electron spectra during the large solar particle events of October-November 2003. *Journal of Geophysical Research*, 110(A09S10), doi:10.1029/2005JA011038

Norman, R. B., Mertens, C. J., & Slaba, T. C. (2016). Evaluating galactic cosmic ray environment models using RaD-X flight data. *Space Weather*, 14, 764-775, doi:10.1002/2016SW001401

O'Neill, P. M., (2010). Badhwar-O'Neill 2010 galactic cosmic ray flux model – Revised. *IEEE Transactions on Nuclear Science*, 57(6), 3148-3153.

Press, W. H., Teukolsky, S. A., Vettering, W. T., & Falnnery, B. P. (1992). *Numerical recipes in Fortran: The art of scientific computing (2nd ed.)*. New York: Cambridge Press.

Singleterry Jr., R. C., Shinn, J. L., Wilson, J. W., Maiden, D. L., Thibeault, S. A., Badavi, F. F., et al. (1999). Aircraft radiation shield experiments – preflight laboratory testing (NASA/TM-1999-209131). Hampton, VA: NASA Langley Research Center.

Smart, D. F., & Shea, M. A. (2005). A review of geomagnetic cutoff rigidities for earth-orbiting satellites. *Advances in Space Research*, 36, 2012-2020.
Slaba, T. C., Blattnig, S. R., Clowdsley, M. S., Walker, S. A., & Badavi, F. F. (2010). An improved neutron transport algorithm for HZETRN (NASA/TP-2010-216199). Hampton, VA: NASA Langley Research Center.
Slaba, T. C. (2013a). Faster heavy ion transport for HZETRN (NASA/TP-2013-217803). Hampton, VA. NASA Langley Research Center.
Slaba, T. C., Blattnig, S. R., Reddell, B., Bahadori, A., Norman, R. B., & Badavi, F. F. (2013b). Pion and electromagnetic contribution to dose: Comparisons of HZETRN to Monte Carlo and ISS data. *Advances in Space Research*, 52, 62-78.
Slaba, T. C., & Stoffle, N. N. (2017). Evaluation of HZETRN on the Martian Surface: Sensitivity tests and model results. *Life Science and Space Research*, 14, 29-35.
Slaba, T. C., & Whitman, K., (2020a). The Badhwar-O'Neill 2020 GCR model, *Space Weather*, 18, e2020SW002456, https://doi.org/10.1029/2020SW002456
Slaba, T. C., Wilson, J. W., Werneth, C. M., & Whitman, K., (2020b). Updated deterministic radiation transport for future deep space mission. Life Sciences in Space Research, 27, 6-18.
Stormer, C. (1965). *The polar aurora*. Oxford: Clarendon Press.
Straume, T., Mertens, C. J., Lusby, T. C., Gersey, B., Tobiska, W. K., Norman, R. B., et al. (2016). Ground-based evaluation of dosimeters for NASA high-altitude balloon flight. *Space Weather*, 14, 1017-1031, doi:10.1002/2016SW001406
Tobiska, W. K., Bouwer, D., Smart, D., Shea, M., Bailey, J., Didkovsky, L., et al., (2016). Global real-time dose measurements using the Automated Radiation Measurements for Aerospace Safety (ARMAS) system. *Space Weather*, 14, 1053-1080, doi:10.1002/2016SW001419
Townsend, L. W., Zapp, E. N., & Hoff, J. L. (2003). Carrington flare of 1859 as a prototypical worst-case solar energetic particle event. *IEEE Transactions on Nuclear Science*, 50(6), 2307-2309.
Townsend, L. W., Stephens Jr., D. L., Hoff, J. L., Zapp, E. N., Moussa, H. M., Miller, T. M., et al. (2006). The Carrington event: Possible doses to crews in space from a comparable event. *Advances in Space Research*, 38, 226-231.
Townsend, L. W., Adams, J. H., Blattnig, S. R., Clowdsley, M. S., Fry, D. J., McLeod, C. D., et al. (2018). Solar particle event storm shelter requirements for mission beyond low Earth orbit. *Life Sciences in Space Research*, 17, 32-39, https://doi.org/10.1016/j.lssr.2018.02.002
Tsyganenko, N. A. (1989). Determination of magnetic current system parameters and development of experimental geomagnetic field models based on data from IMP and HEOS satellite. *Planetary and Space Science*, 37, 5-20.
Tsyganenko, N. A. & Sitnov, N. I. (2005). Modeling the dynamics of the inner magnetosphere during strong geomagnetic storms. *Journal of Geophysical Research*, 110, A03208, doi:10.1029/2004JA010798
Tylka, A. J., Cohen, C. M. S., Dietrich,W. F., Lee, M. A., Maclennan, C. G., Mewaldt, R. A., et al. (2005). Shock geometry, seed populations, and the origin of variable elemental composition at high energies in large gradual solar particle events. *The Astrophysical Journal*, 625, 474-495.
Tylka, A. J., & Lee, M. A. (2006). Spectral and compositional characteristics of gradual and impulsive solar energetic particle events, in solar eruptions and energetic particles. In N. Gopalswamy, R. Mewaldt, & Torsi, J. (Eds), *Solar Eruptions and Energetic Particles*, *Geophysical Monograph Series* (Vol.165, pp. 263-274). Washington, DC: American Geophysical Union.
U. S. Standard Atmsophere, 1976 (1976). NASA-TM-X-74335. Washington, DC: National Oceanic and Atmospheric Administration, National Aeronautics and Space Administration, and United States Airforce.
Van Allen, J. A. (1968). Particle description of the magnetosphere. In *Physics of the Magnetosphere* (Vol. 10, pp. 147-217). New York, NY: Springer-Verlag.

Wilson, J. W., Townsend, L. W., Schimmerling, W., Khandelwal, G. S., Khan, F., Nealy, J. E., et al. (1991). Transport methods and interactions for space radiation (NASA RP-1257). Washington, DC: NASA.

Wilson, J. W., Badavi, F. F., Kim, M.-H. Y., Clowdsley, M. S., Heinbockel, J. H., Cucinotta, F. A., et al. (2002). Natural and induced environment in low earth orbit (NASA/TM-2002-211668). Washington, DC: NASA.

Wilson, J. W., Tripathi, R. K., Mertens, C. J., Blattnig, S. R., Clowdsley, M. S., Cucinotta, F. A., et al. (2005). Verification and validation of High charge and Energy (HZE) transport codes and future development (NASA/TP-2005-213784). Washington, DC: NASA.

Wu, H., Atwell, W., Cucinotta, F. A., & Wang, C.-H. (1996). Estimate of space radiation-Induced cancer risks for International Space Station orbits (NASA TM-104818). Linthicum Heights, MD: NASA Center for AeroSpace Information.

Xapsos, M. A., Barth, J. L., Stassionopoulos, E. G., Messenger, S. R., Walters, R. J., Summers, G. P., & Burke, E. A. (2000). Characterizing solar proton energy spectra for radiation effects applications. *IEEE Transactions on Nuclear Science*, 47(6), 2218-2223.

Zhang, S., & Jin, J. (1996). *Computation of special functions*. New York: John Wiley and Sons, Inc.